Università degli Studi di Padova

Dipartimento di Ingegneria Industriale
Corso di Laurea in Ingegneria Energetica

Tesi di Laurea Magistrale

Unsteady CFD analysis of a wind turbine operating under gust conditions

Laureando:
Luca Menegozzo

Relatore:
Prof. Ernesto Benini

Correlatore:
Ing. Andrea Dal Monte

Anno accademico 2015/2016

"There are no facts, only interpretations"

Friedrich Nietzsche

List of Figures

List of Tables

Contents

Summary

A wind turbine has to face strongly variable operating conditions during its lifetime. Thus, despite the technological advancements of the last decades, design and general operative assessment are still very challenging steps. It is therefore necessary to improve the knowledge on the interaction between machine and airflow.

The transient character of atmospheric conditions makes most of the available empirical models inadequate to describe the 3D aerodynamics of a wind turbine. Field testing can provide useful measurements, but the disturbance due to random turbulence and variable environmental conditions has a great influence. Aerodynamic models based on the Blade Element Momentum method (BEM) are straightforward, make good estimations and require a rather small computational effort, but they need an empirical input, and present some limitations in the prediction of unsteady phenomena. In fact for separated flows or highly 3D effects BEM theory does not provide accurate predictions due to restrictions inherent to the 2D hypotheses. On the other side, Computational Fluid Dynamics techniques (CFD) are much more flexible, with increased computational cost though. However the available capacity of modern calculators makes CFD an extremely powerful numerical tool that can handle a huge variety of engineering cases, providing reliable estimations with a relatively affordable cost.

The present work aims to study the general behaviour a wind turbine of known characteristics operating in steady and unsteady conditions using a validated CFD model. A necessary overview about the underlying physics and the reference experiment for the validation are presented in Chapter 1. The well documented Unsteady Aerodynamics Experiment by NREL was reproduced in order to confirm the steady computations. The geometrical model and the computational grid employed are described in Chapter 2. In Chapter 3 the settings adopted for the solver and the results of the steady validation are discussed. Pressure distributions, stall development and aerodynamic torque are reported. Thanks to the symmetry hypothesis only one blade was considered, together with Multiple Reference Frame approach (MRF).

In the second part of the work, the influence of a wind gust on the operation of the wind turbine is analysed. An introduction on the general characterization of wind gusts, on their detection and their modelling is presented in Chapter 4. The unsteady simulations of the wind turbine both in operating and parked conditions were performed, considering a gust model proposed in IEC 61400-2 standard. The moving mesh method was necessarily applied. Model adjustments are discussed in Chapter 5, along with the results regarding torque, loads and flow dynamics.

- I -

Introduction

After a brief overview on wind energy and the governing physics, the Unsteady Aerodynamics Experiment is described. Based on this test, a turbine model validation was performed, as discussed in the next chapters. An overview on the analysed researches based on the same wind turbine is proposed, followed by the explanation of the necessary flow equations and turbulence models.

Wind energy

Wind power is not only a clean alternative, but also a growing trend of the world's energy systems and markets. The installation of new wind turbines experienced a great increase in the last years. Up to June 2016 wind energy production was able to cover 4.7% of the global electricity demand. The actual installed capacity of 457 GW is predicted to reach 500 GW for the end of 2016, as plotted in Figure 1.1, where the trend of the cumulate power is reported for the last year [1]. This corresponds to a growth of 16.1% on annual basis. Investments of around 100 billions of euros were registered in 2015, so 4% more than the year before. Only in the EU wind power corresponds to the 30% of the new power installations since 2000, and covers 11.4% of the European electricity consumptions [2]. Moreover to attempt a reduction of the global warming and of the human environmental impact an energy conversion to renewable solutions is an urgent necessity.

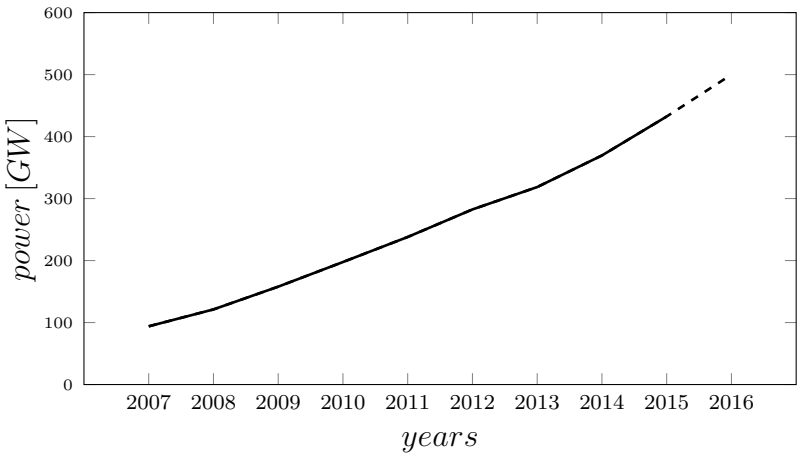

Figure 1.1: *worldwide installed wind capacity, prediction for the end of 2016* [1].

A wind turbine converts kinetic energy of the airflow to mechanical torque by its rotation, and then in electrical power [3]. The maximum ideal conversion limit from wind power P_0 to mechanical power P, expressed by Equation 1.1, is 0.593, according to Betz (1919). A is the area swept by the turbine, u the wind speed and ρ its density. In non-ideal conditions number of blades, air friction and the rotation of the wake region lower this limit. The best performing modern HAWTs reach power coefficients around 0.45 [4]. Furthermore this is a maximum value, since it depends on the tip speed ratio, or the ratio between the speed of the blade tip and the undisturbed wind velocity.

Airfoil-shaped blades are designed in order to create a pressure difference at their sides as they interact with the airflow, determining high pressure in the upper side and low pressure in the lower side, namely pressure side and suction side. The aerodynamic effect on the blade is the generation of a pressure distribution all over its surface. In Figure 1.2 the forces acting on an airfoil are shown in terms of dimensionless coefficients. The pressure integration gives the lift force L, whereas the combination of air friction and pressure drag cause the drag force D. The two vectors L and D are respectively perpendicular and parallel to the relative velocity V_r. Once decomposed, these forces correspond to a tangential and a normal component, referring to the plane of rotation. The tangential component times the radial distance from the center of rotation corresponds to the aerodynamic torque at the given radius, whereas the normal component is the thrust force in the direction of the incoming wind.

Wind turbine blades are often characterized by a radial variation of the twist angle and of the chord lenght, as well as by a global pitch angle, to help the most efficient interaction between the profile and V_r, which changes in direction and magnitude moving from hub to tip. The angle between the chordwise direction and the plane of rotation is the angle of attack α, proportional to the incoming wind speed. Higher attack determines a greater lift effect, up to a maximum at the stall onset, where drag increases and lift drops. For the detailed theory an appropriate literature is suggested [5].

$$C_P = \frac{P}{P_0} = \frac{P}{\frac{1}{2}\rho A u^3} \tag{1.1}$$

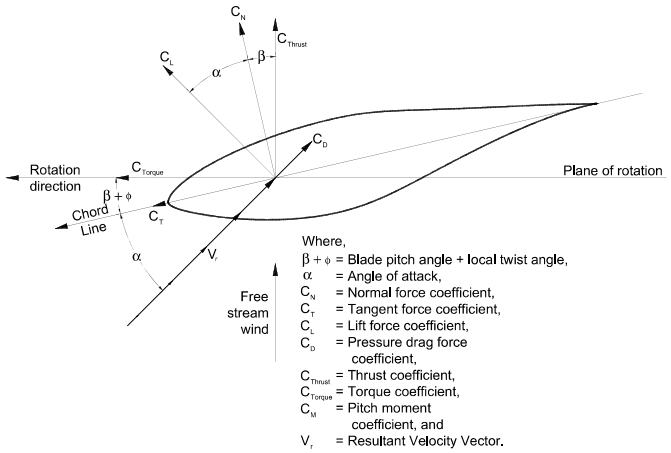

Figure 1.2: *aerodynamic forces acting on a wind turbine airfoil* [6].

The experiment

During field operation wind turbines experience far more complex conditions if compared to the theoretical models and 2D airfoil simulations. This happens due to the arising of 3D unsteady effects, as the radial development of stall and the vortex generation. Inflow anomalies as wind variations and surrounding obstacles make field data not suitable to show accurately the influence of those effects. Moreover a field test is much more complicated to reproduce in a numerical way, due to the cited irregular and random conditions. Wind tunnel testing instead can provide reliable data, valid to understand 3D phenomena and their implications on the performance of the machine. They can in fact be used as a valuable input for CFD simulations, since the conditions are well known.

The CFD model developed in this thesis was validated against a wind tunnel dataset. Measurements were obtained in the Unsteady Aerodynamic Experiment (UAE) carried out by the National Renewable Energy Laboratory (NREL) of US energy department [6]. The experiment, completed in May 2000, focused on giving aerodynamic and structural results for a full-scaled HAWT in controlled operating conditions. The world's biggest wind tunnel was employed, in the NASA's Ames Research Center featuring a 24×36 m test section. This allowed the full-scale testing. NREL had developed the *Phase VI* constant speed, constant pitch, stall-regulated wind turbine for this experiment. The machine is characterized by a two-bladed rotor of 10 m diameter, and hub height of 12.2 m, so that it was located in the tunnel centreline. Rated rotational speed is 72 rpm and rated power is 19.8 kW. Twisted and tapered blades are shaped using S809 airfoil[1]. Below 0.25 span there is a cylindrical section for the hub attachment, and a transition section from circular to airfoil shape, while from that radius the aerodynamic profiles begin. The linear taper ratio is 2.1, whereas the twist is defined by a non-linear variation, as reported in Figure 1.3. Pitch, yaw and cone angle are manually set by operators. Turbine geometrical and technical data are summarized in Table 1.1.

blade radius $[m]$	5.029	hub height $[m]$	12.20
twist axis $[\%\ chord]$	30	airfoil	S809
rated power $[kW]$	19.80	rated rpm	71.63
power regulation	stall	cut-in speed $[m/s]$	6

Table 1.1: *turbine geometrical and technical data* [6].

tip pitch angle [°]	3	global pitch angle [°]	4.815
yaw angle [°]	0	cone angle [°]	0
wind direction	upwind	blade tip	baseline

Table 1.2: *sequence S turbine settings* [6].

[1] See Appendix A.

Once completed the experiment, NREL revealed the measured data to verify many predictions from computational BEM and CFD codes developed by experts around the world [7]. Of the several tests performed in different conditions, *Sequence S* case is here considered, that is 3° tip pitch and 0° yaw and cone angles. This means that the blade was rotated of approximatively 5° towards feather around its twist axis. Nevertheless these are the turbine standard operating conditions. The test ran with 6 wind speed values from 7 m/s to 25 m/s. Settings are reported in Table 1.2.

To measure the pressure field on the blade surface 22 pressure taps were installed at 5 main radial positions, which are 0.30, 0.47, 0.63, 0.8 and 0.95 span. Sensors were clustered around the profile's leading edge, as shown in Figure 1.3. Measured pressures p were normalized with the profile stagnation pressure, considered equal to the maximum measured pressure p_{max} at the same span position. This led to the calculation of pressure coefficients c_p, as expressed by Equation 1.2, for the tap i at radius r. The same steps were applied in the CFD simulation, as explained in Chapter 3.

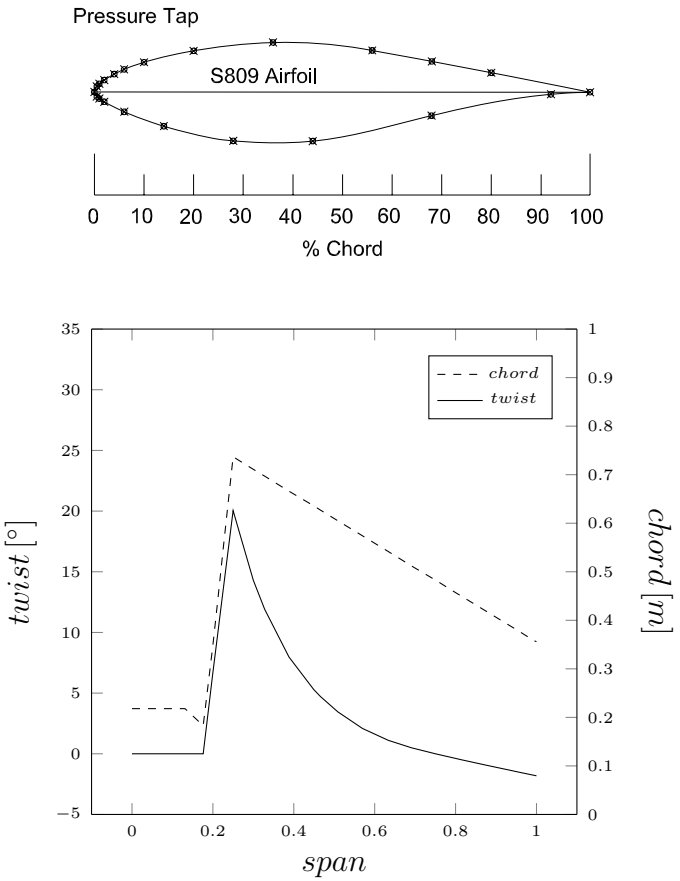

Figure 1.3: *S809 profile with pressure taps, and spanwise distribution of twist and chord* [6].

$$c_{p,i}(r) = \frac{p_i(r)}{p_{max}(r)} \tag{1.2}$$

Background

Many CFD simulations of wind turbines concern the *Phase VI* datasets. Thanks to its fully documented conditions and results, the UAE is a benchmark in this field, as it allows the validation of different numerical models. The reference works on this theme are presented below. Main differences exist in the methods, regarding solver, turbulence model, mesh, and symmetry hypotheses. In the following summary, if not mentioned, $k-\omega$ SST turbulence model is implied.

Mo and Lee [8] analyzed the problem using ANSYS Fluent incompressible solver. Very good matching with the experiment is found, both for stall developement and pressure distributions, whereas the shaft torque is underestimated for medium-high wind speeds. y^+ was kept around 7. Sørensen et al. [9] adopted the incompressible RANS equations too, but employed the *EllypSys3D* solver. Two grids were tested to study the tunnel influence, with $y^+ < 2$. Even though high errors are detected in the calculated shaft torque, stall and pressures are correctly predicted for all the wind speeds, except for 10 m/s.

Le Pape and Lecanu [10] applied the *elsA* compressible solver, primarily developed for helicopter rotors. To prevent RANS numerical issues due to low Mach numbers a low-speed preconditioning was activated. The blade root influence was studied, with y^+ value around 1. While good results are found for low wind speeds, convergence problems arose for medium-high velocities. A poor agreement resulted in the CFD torque values. Another compressible RANS calculation was performed by Yelmule and Anjuri [11] using ANSYS CFX. A very fine matching is shown for power values, except for 10 m/s, due to the onset of stall, and pressure coefficients are in good agreement. 2D airfoil calculations are performed too. Huang et al. [12] chose the Spalart-Allmaras one equation model instead, whose known limitations in predicting the location of flow separation are pointed out. A custom compressible solver was employed, with low speed preconditioning and $y^+ < 2$. Pressure distributions match the measurements especially for low and high wind speeds, and the torque trend is correctly predicted.

While all the previously discussed articles modelled one blade, emphatizing the 180° geometrical symmetry and employing only structured meshes in steady conditions, other works considered the whole turbine rotor and adopted unstructured moving meshes. Sezer-Uzol and Long [13] used PUMA2 unsteady compressible solver with implemented wall functions. They analyzed the yawed and non-yawed conditions, and the results show a good trend. LES computations and noise predictions are also included. Song and Perot [14] performed simulations with an OpenFOAM CFD code and Spalart-Allmaras turbulence model. PIMPLE incompressible transient algorithm was adopted, with $y^+ < 5$. A good agreement is found for the pressures, and torque calculations reflect its general trend.

Governing equations

The point of CFD analysis is discretization. During the simulation the flow motion is not solved in any position of the domain, but in the center of all the fluid elements of the computational grid. The basis of the numerical method applied stands in the Navier-Stokes equations set (1822), which include some pillar principles of physics: the conservation of mass, momentum and energy. The incompressible fluid approximation has been employed, as the involved Mach number values are low enough. The conventional limit is considered at 0.3, and for the highest wind speed simulated in this work a value around 0.1 has been computed. Therefore the flow velocity doesn't introduce significant changes in air temperature or in its density ρ. This is a common approach not only for liquids but even for air flowing at moderate speeds [15].

Mass conservation, or continuity, states that the increase of the mass inside the fluid element is equal to the net rate of mass flow through the element. Thanks to the incompressibility hypothesis and to the absence of mass sources, continuity is reduced to Equation 1.3.

The momentum conservation is as a consequence of Newton's laws. The increase of momentum of the fluid particle corresponds to the sum of forces on the particle itself. The principle is expressed by Equation 1.4, being μ the constant dynamic viscosity, $\vec{F}$ the external forces and $\vec{g}$ the gravity acceleration. The $\mu\nabla^2\vec{u}$ term in the right part of the equation is the divergence of the deviatoric stress tensor τ, as explained in Equation 1.5. This is the simplified form thanks to incompressible and Newtonian fluid assumptions.

Also, if ρ is constant, energy equations are an independent set, not correlated to continuity and momentum [16]. As the analysed situation doesn't treat heat transfer, these equations are not considered in the model. The Navier-Stokes equations presented are expressed in absolute formulation, so all the variables are referred to an inertial reference frame. If the majority of the fluid domain is rotating, then the relative formulation is suggested.

$$\nabla \cdot \vec{u} = 0 \tag{1.3}$$

$$\frac{\partial \rho \vec{u}}{\partial t} + \rho(\vec{u} \cdot \nabla)\vec{u} + \nabla p = \mu\nabla^2\vec{u} + \rho\vec{g} + \vec{F} \tag{1.4}$$

$$\nabla \cdot \tau = \mu\nabla \cdot \left[\nabla\vec{u} + (\nabla\vec{u})^T\right] = \mu\nabla^2\vec{u} \tag{1.5}$$

Since the flow to be solved is characterized by turbulence, the variables experience a continuous random fluctuation in time. Any of these variables ϕ can be represented by an average value $\overline{\phi}$ plus an oscillating term ϕ', as shown in Equation 1.6. The $\overline{\phi}$ term is a time-averaged value, obtained with the Reynolds operator (1895) of Equation 1.7. If this method is applied to the previous relations, Reynolds averaged Navier-Stokes (RANS) equations are obtained.

The solutions are average values in the time interval Δt, which is big enough compared to molecular scales causing the momentum transfer, but much smaller than the characteristic scales of the analysed problem. This procedure of continuum approximation strongly reduces the computational effort when the detailed solution of turbulence structures is not of first importance, and when the mean flow has a dominant effect on the anisotropy of turbulence. Moreover, the direct calculations of turbulent fluctuation for smaller scales, like Large Eddy Simulations (LES) and Direct Numerical Simulations (DNS), is still prohibitive for most of the practical applications.

Nevertheless additional terms appear due to the averaging process: the Reynolds stresses, which stand for the convective momentum transfer of turbulent eddies due to the velocity fluctuation. They cannot be neglected because their characteristic scales are similar to the ones of the solution. So further equations are necessary to relate these stresses to the mean motion, and close the RANS equations system. The most common closure method is the Boussinesq assumption (1877) that turbulence is isotropic and its stresses act as the viscous ones, except for the molecular viscosity ν, which is replaced by eddy viscosity ν_t [17]. In this way the same computational codes can be used for both laminar and turbulent calculations, by changing the properties accordingly.

By analogy with the kinematic theory of gases, which states that ν is proportional to the mean molecular path times the average molecular speed, ν_t is treated as proportional to characteristic turbulence length $\mathcal{L}$ and velocity $\mathcal{U}$ scales, as explained in Equation 1.8. Furthermore these scales correspond to size and velocity of eddies, and they are often included in RANS equations by means of turbulence models, as further discussed.

$$\phi = \overline{\phi} + \phi' \tag{1.6}$$

$$\overline{\phi} = \frac{1}{\Delta t} \int_{t_0}^{t_0+\Delta t} \phi dt \tag{1.7}$$

$$\nu_t = \frac{\mu_t}{\rho} \propto \mathcal{L}\mathcal{U} \tag{1.8}$$

Turbulence

Since the *Phase VI* turbine is stall-regulated, flow separation and adverse pressure gradients are expected even at medium wind velocities. The turbulence model choice is thus a fundamental step that significantly influences numerical results.

Turbulence models are employed to obtain an estimation of the Reynolds stresses and close the RANS system of equations. They can be roughly divided in one-equation two-equations models, although more-than-two-equation-models are available today. In one-equation models, like Spalart-Allmaras, the differential transport equation for turbulent kinetic energy k is solved to determine $\mathcal{U}$, whereas $\mathcal{L}$ is algebraically defined in terms of geometrical parameters. In two-equations modes, like $k-\epsilon$ and $k-\omega$, in addition to the k equation another one is solved, determining either the rate of k dissipation, ϵ, or the specific dissipation $\omega = k/\epsilon$. In practical terms, the near-wall flow behaviour is well predicted by $k-\omega$ model, since its original purpose is the application to boundary layers [18]. However, due to its free-stream sensitivity, there's no solution independence in the bulk flow. It can be obtained with the $k-\epsilon$ model instead, which is accurate for free stream and high Re flows. In the near-wall regions wall functions are applied, giving a fast but less precise calculation.

One of the most widespread turbulence models employed in wind turbine simulations is the Menter's $k-\omega$ SST model. It is a combination between the two previously mentioned models. A blending function ensures the gradual variation from $k-\omega$ to $k-\epsilon$ moving away from the wall, such that advantages are taken from both. This model was adopted in this work: the most important reason is that the study of the modelled turbine operating in variable wind conditions may lose significance if the near-wall bounded effects, where the most intense gradients occur, are treated in a rather arbitrary way.

Inside the boundary layer velocity profiles can be correctly modelled in the sub-layer, where viscous shear stress is the governing force. The profiles are known in the log layer and outer layer too, where turbulence gains strength, leading to fully developed turbulent flow. The physics of the transition region in between is not completely understood, and no reliable models have been developed yet. The placement of the first cell node above the wall is thus extremely meaningful in terms of solution. Its height y over the blade surface can be referred in terms of dimensionless wall distance y^+, defined by Equation 1.9, being u^* the wall friction velocity and τ_w the wall shear stress. Briefly, for $k-\omega$ SST model:

$$y^+ = \frac{u^* y}{\nu} = \sqrt{\frac{\tau_w}{\rho}}\frac{y}{\nu} \tag{1.9}$$

- $y^+ < 5$: the first node is in the viscous sub-layer, $k-\omega$ model is used.
- $5 < y^+ < 30$: the first node is in the buffer layer, where no accurate model stands.
- $y^+ > 30$: the first node is in the log layer or above, and $k-\epsilon$ is employed. The boundary layer behaviour is modelled by a wall function.

- II -

The model

The development and validation of the wind turbine model is here presented. After the geometrical definition of the examined wind turbine, the 3D geometrical characterization is explained. The building process of the computational grid is then discussed.

Geometry

The development of the *Phase VI* model started from its geometry. For computational effort reasons only half of the rotor was analysed in the first part of the work, taking advantage of the 180° symmetry of the two-bladed turbine and the uniform inflow conditions. The influence of the wind tower was neglected.

Following the geometrical data in the official NREL report a 3D SolidWorks blade model was created. The transition section near the hub attachment was simplified using with the *loft* tool between the circular attachment section and the first airfoil section, due to the lack of a completely defined geometry. The nacelle was approximated by a 0.508 m radius half-cylinder with two hemispherical elements at the ends. This radius value is the radial distance at which the blades are attached to the hub, or the root section. The blade surface was divided in 10 sections, equally spaced in spanwise direction and starting from 25% span, thus each one is 7.5% span wide. The sectioning is visible in Figure 2.1. The inboard region of the blade was divided in two elements too. To avoid the formation of low quality mesh elements around the S809 sharp trailing edge, it was cut at 99% of the chord length. Trailing edges are rounded for constructive issues, but for CFD purpose this percentage depends also on the resulting mesh quality.

The whole control volume is shown in Figure 2.2, being the blade radius R the reference length. The geometrical model has the z axis as the blade twist axis, and the y axis and tunnel centreline. The blades rotate about y axis, in counter-clockwise direction if seen from the incoming wind. Blade and nacelle volumes are included in an half-cylinder inner domain, which is enclosed in an half-cylinder outer domain. The control volume has a front section nearly equal to the wind tunnel one, with 15 m radius. It has a total length of 120 m, with the blade positioned at 40 m from the front section and 80 m from the rear one, to ensure negligible wake effects at the outlet.

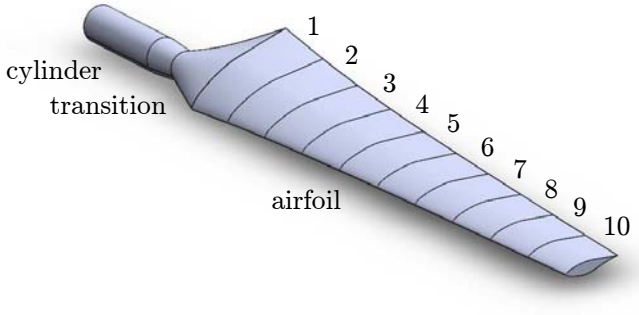

Figure 2.1: *SolidWorks turbine blade.*

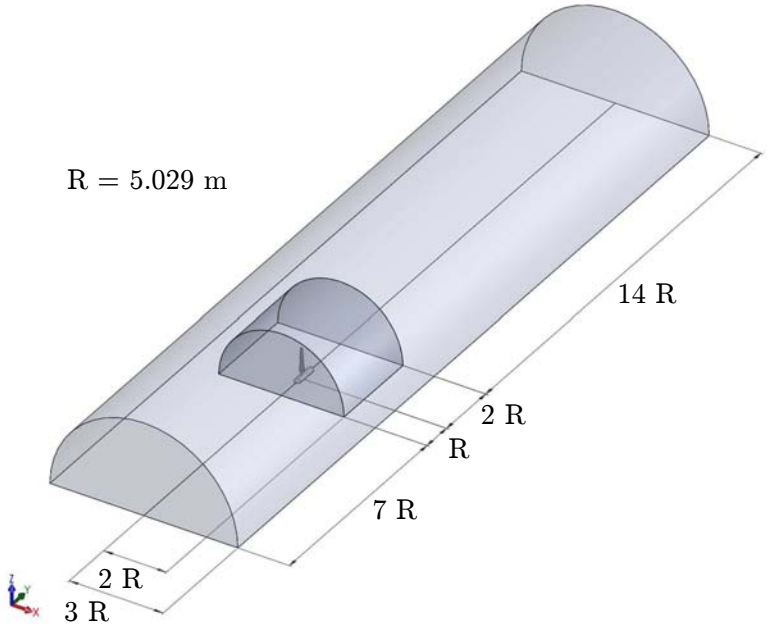

Figure 2.2: *SolidWorks control volume. Wind direction: positive y.*

Mesh

The geometrical model was directly imported in Pointwise 17.3, without conversions, to provide a wireframe for the mesh construction. The grid can be divided in 4 main regions: outer domain, inner domain, blade surface and boundary layer. This grid has a total of 4.2 million mixed elements. In Figures 2.3, 2.4 and 2.5 the main views are depicted. The cited regions are explained below.

- *Outer domain*: all the surface meshes are unstructured, with 0.85 boundary decay. The two bottom surfaces are built with the *periodic* function, to grant the necessary symmetry for the solver periodicity conditions. The volume mesh is coarse with 0.1 million tetrahedral elements of 1.5 m average size. The previous boundary decay was applied even for the volume mesh.

- *Inner domain*: surfaces and volume were meshed as in the outer domain. Cell size reduces while approaching to boundary layer of the blade. The 2.8 million elements tetrahedral volume elements are refined to an average size of 36 mm.

- *Blade surface*: structured mesh was adopted for all the blade surfaces, except for the tip, where an unstructured mesh with 0.9 boundary decay was used. After some sensibility tests and accordingly to previous works, 250 nodes were positioned around the airfoils, 125 for each side. The straight trailing edge cut is thus composed by 2 nodes, with a resulting edge length ranging from 0.4 to 0.9 mm. A slight clustering was applied at leading and trailing edges, increasingly towards tip, up to 2 mm in both spanwise and chordwise directions. To avoid the formation of very skewed volume elements near the trailing edge region, but keeping at the same time a low total cell number, 350 nodes were positioned on the whole blade in spanwise direction. The most problematic zone from this point of view was the highly twisted transition section.

- *Boundary layer*: the blade's boundary layer consists of 1.3 million mixed hexahedral and prismatic elements, being the latter over the tip surface. The *extrude* function was applied to the blade surface, with 15 steps and a 1.2 grow factor. The height of the first boundary layer cell was tuned in order to keep $y^+ < 2$ over the entire blade surface for all the examined wind speeds. Therefore the first extrusion step was set to $1 \cdot 10^{-5}$ m up to the 7th blade sections, while it was lowered to $0.5 \cdot 10^{-5}$ m for the last 3 sections. In the end a maximum value of 1.5 for 25 m/s was observed. This ensures the coherent application of the $k - \omega$ SST turbulence model.

Pointwise allows also to initialize boundary and volume conditions for various solvers, and in this case ANSYS Fluent was selected. Each spanwise section was divided into pressure side, suction side and trailing edge *wall* conditions. Nacelle, inlet and outlet were set to *wall*, *velocity inlet* and *pressure outlet*. The bottom and the lateral enclosing surfaces were initialized as *symmetry*.

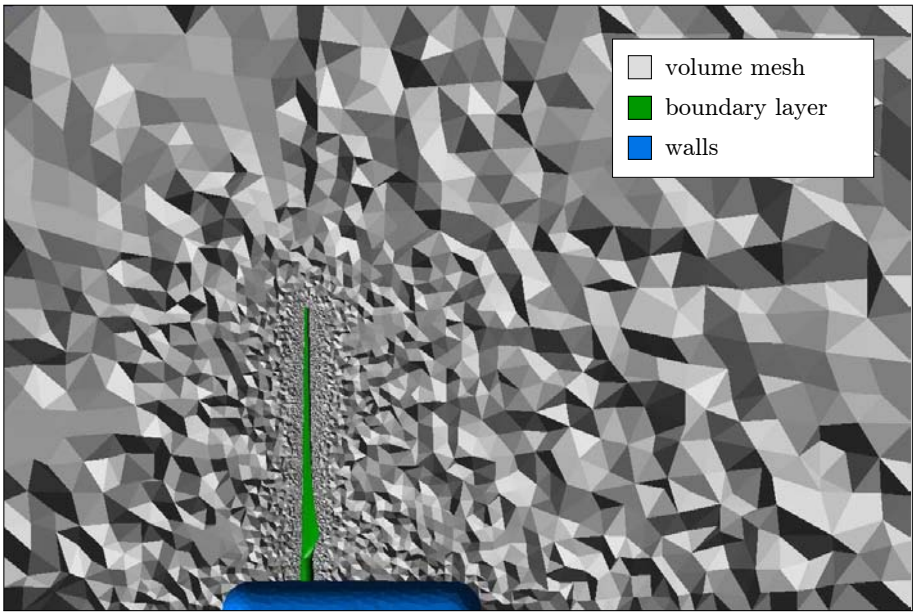

Figure 2.3: *inner domain, $x = 0$ section, side view towards $x < 0$.*

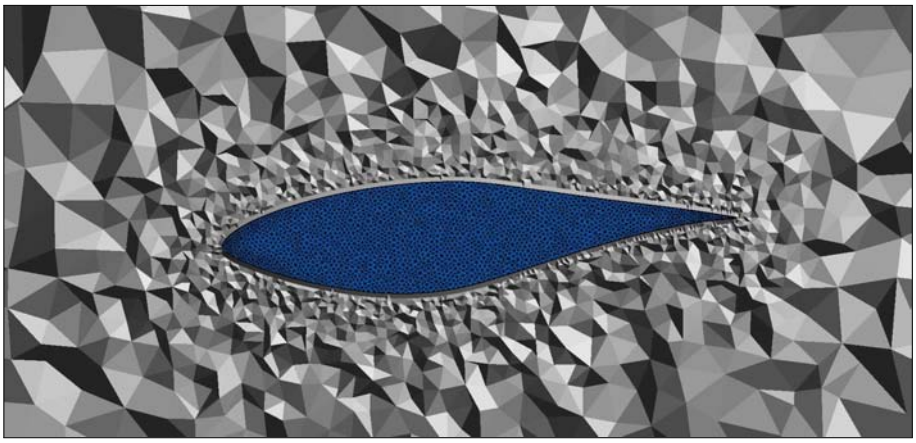

Figure 2.4: *tip surface mesh, $z = 5.029$ section, top view.*

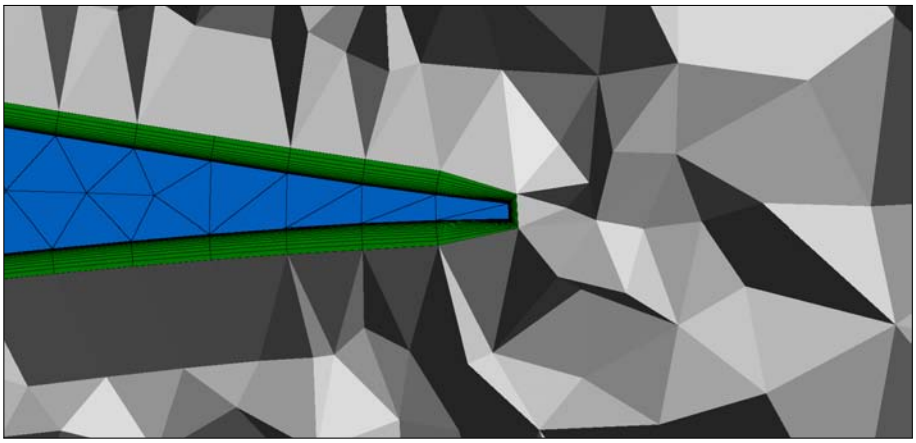

Figure 2.5: *tip surface, detail of the trailing edge and boundary layer.*

- III -

Steady CFD validation

The environmental settings for the steady simulations were imposed following the experimental conditions. The preferences about physical values, boundary conditions, employed algorithm and solution parameters are explained. In the end, the results are presented and commented along with the measured values, both for pressure and torque calculations.

Solver setup

The computational mesh was imported in ANSYS 16.1 Fluent pre-processor. Air was considered as an incompressible fluid, as already stated, and its density was set to the experimental value for each wind speed. The MRF option was applied to the inner domain, using the measured turbine rotational speed. More informations about MRF are further reported. All the relevant values employed are reported in Table 3.1, together with the wind tunnel static pressure for each simulated case. All the pressure measurements performed in the experiment were referred to the tunnel static pressure p_E. Fluent allows to define a *reference pressure* Δp_F, which is the difference added to the *operative pressure* p_0, kept as default to atmospheric value. The reference value was thus set to the difference between p_E and the atmospheric value p_0. Therefore, according to Equation 3.1, in the CFD simulation the static pressure p_F was equal to the measured tunnel static pressure of the experiment.

$$p_F = p_0 + \Delta p_F = p_0 + (p_E - p_0) = p_E \tag{3.1}$$

speed $[m/s]$	density $[kg/m^3]$	rpm	pressure $[Pa]$
7.016	1.246	71.867	101959.328
10.047	1.246	72.096	101894.813
13.069	1.227	72.094	101410.336
15.098	1.224	72.062	101365.945
20.131	1.221	72.009	101204.070
25.109	1.220	72.162	101025.648

Table 3.1: *sequence S wind speeds, densities, rotational speeds and tunnel static pressures* [6].

Boundary conditions are represented in Figure 3.1. *No slip wall* condition was set for blade and nacelle, with *motion bc moving* option, to account for the virtual rotation of MRF mode. For the bottom surfaces the rotational *periodic* condition was used, fixing 180° angle with the *repair periodic* tool. In fact a slightly different angle was initially detected by Fluent. *Velocity inlet* condition was applied to the front section, with wind direction normal to the surface and measured value for the wind speed. Turbulent intensity was lowered to 0.5%, instead of the Fluent standard value of 5%, to simulate the wind tunnel controlled inflow conditions [7]. Zero gauge pressure was set to the the rear section of the control domain with the *pressure outlet* condition, and the same turbulence parameters of the inlet section were applied. The far field lateral surface of the outer domain was kept to the *symmetry* condition set in Pointwise.

The *pressure-based* steady solver with *coupled* algorithm was engaged. This means that the RANS equations of continuity and momentum are used to derive a pressure correction equation, such that the corrected pressure field satisfies continuity [18]. The chosen algorithm solves a coupled system with momentum and pressure-corrected continuity, accelerating convergence, but also requiring almost twice the computational memory compared to the segregated algorithm, in which the equations are solved in a separate way.

Discretization for pressure, momentum, k and ω was imposed to second order. A maximum allowable Courant number of 40 was chosen, accordingly to Fluent advice. Explicit relaxation factors of 0.5 and 10^{-5} residuals were used. A moment monitor was set to check the convergence trend of the moment M_y about y axis, and 10000 iterations were then launched. In the end five control surfaces were introduced at the main spanwise positions, and pressure distributions were plotted in the chordwise direction, using the local twist angle value. A report of the wall forces was also included to evaluate the radial distribution of the moment around y axis, with direction vector pointing upwind.

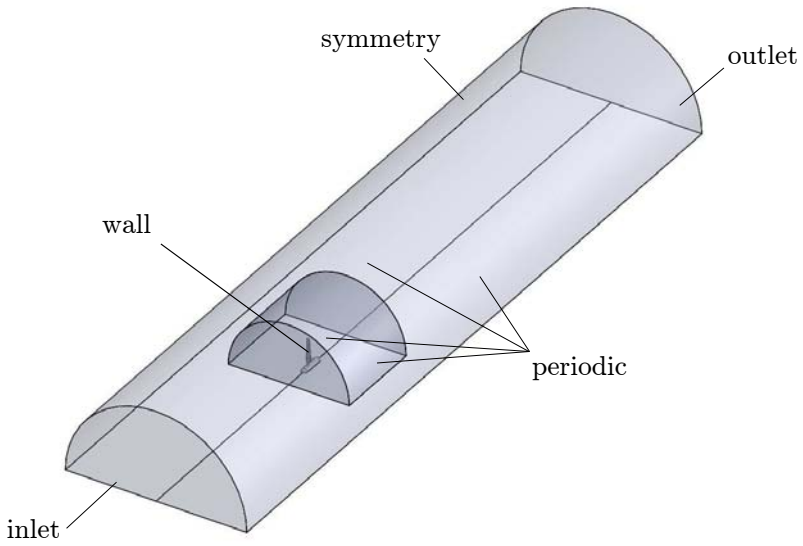

Figure 3.1: *boundary conditions.*

Multiple Reference Frame

By default, Fluent solves the governing flow equations in an inertial reference frame [18]. If moving parts are involved, an unsteady flow character is present. In some cases the flow around the moving region can be solved with approximated steady-state conditions, if a local moving reference frame is considered. Therefore the RANS equations are provided with the additional terms of moving reference frame transformation. If a single reference frame cannot be used, Multiple Reference Frames (MRF) can be defined for various cell zones separated by *interface* boundaries. No settings need to be applied for these interfaces in the MRF approach, unlike in the moving mesh case, as discussed in the apposite section of Chapter 5.

In the analysed case, Navier-Stokes equations were solved using the rotating local reference frame of the rotor for the inner domain cells, whereas the absolute reference frame was adopted for the rest of the control volume. In the interface surfaces between different zones a local reference frame transformation is enabled, to use the flow variables of both zones. The grid is stationary, then a relative motion between zones is not accounted. In the MRF mode, or *frozen rotor approach*, a specific position of the moving region is maintained, and the instantaneous flow field is analysed. In the present case, the blade keeps its vertical position. Although this approach is an approximation, it gives good results if large scale transient events are not expected, saving computational resources and time, and avoiding the mesh motion. In an uniform flow fields, as in the steady validation cases, the blade-fluid interaction is not time-dependent, nor azimuth-dependent, and it can be modelled with a single static position. Moreover, MRF method was also used to provide an initial solution for the unsteady calculations with mesh motion.

Figure 3.2: *Phase VI wind turbine in the AMES wind tunnel.*

Steady results

The results of the steady validation are here discussed. Firstly, the coupled analysis of the surface streamlines on the suction side of the blade and the pressure distributions is proposed, to understand the stall development with the increasing wind speed. Then observations on the pressure and velocity fields around the blade are presented. In the end results regarding the aerodynamic torque are discussed, considering both the integral and the radial values.

Streamlines

In Figure 3.3 the surface streamlines over the blade's suction side are shown for each wind speed, so that the stall process can be analysed. The flow separation starts from the trailing edge region, thus the stall evolution is gradual, and not abrupt, which would be expected if sharp airfoils were adopted. The black vertical lines indicate the five spanwise positions where pressure measurements were performed. It's visible that for 7 m/s the stall is moderate and involves only the lower part of the blade, whereas attached flow runs over the rest. The radial flow due to the centrifugal effect increases noticeably at 10 m/s, with a stronger effect between 0.47 and 0.63 span, influencing also the 0.30 section, and partially the 0.80 too. For 13 m/s and 15 m/s the radial current reaches 0.95 span and the separation is complete up to 0.63 span. For 20 m/s and 25 m/s the blade is operating in fully stalled conditions.

Pressure distributions

Equation 1.2 was used to evaluate the c_p values from the CFD pressures referred to the control surfaces at 0.30, 0.47, 0.63, 0.80 and 0.95 span, as done in the experiment. The results are reported from Figure 3.4 to Figure 3.9. Standard deviations of each pressure measurement are included. The plots have reversed vertical axis, coherently with other works: the airfoil pressure side is thus represented by the lower part of the distribution, and the suction side by the upper one.

A good agreement was generally found with the experimental data, and the overall trends are respected. The 0.30 span position showed the worst accordance, and this may be caused by the influence of the geometry of the transition section and by the stall process. It should be mentioned that the low pressure peak due to the accelerated flow passing around the leading edge after stagnation, and also the suction side pressures in minor part, showed a dependence to the mesh clustering around the leading edge. A sensitivity test was thus performed to find the suitable mesh configuration, monitoring both the pressure peak and the resulting integral torque. Comments to the results for all the wind speeds are now presented.

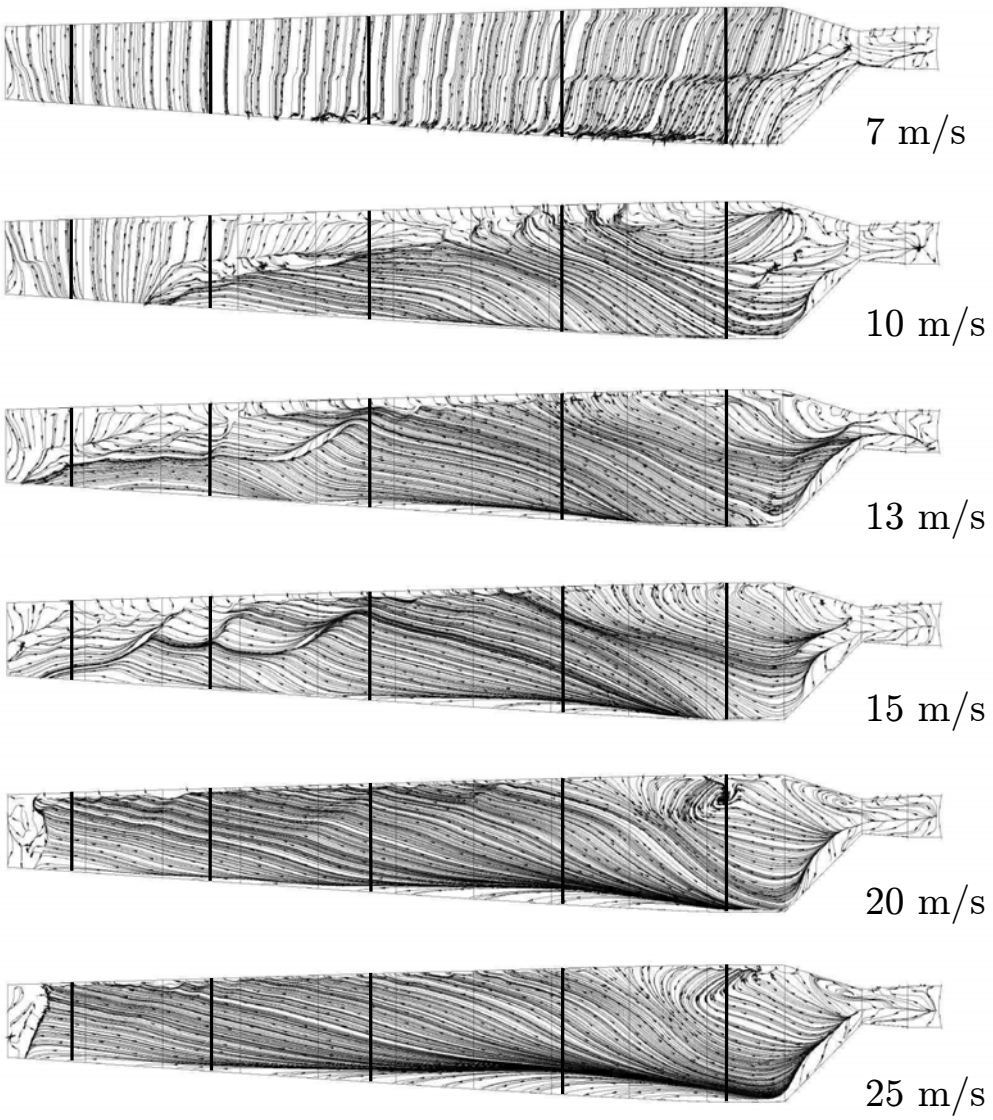

Figure 3.3: *limiting streamlines over the suction side for all the wind speeds.*

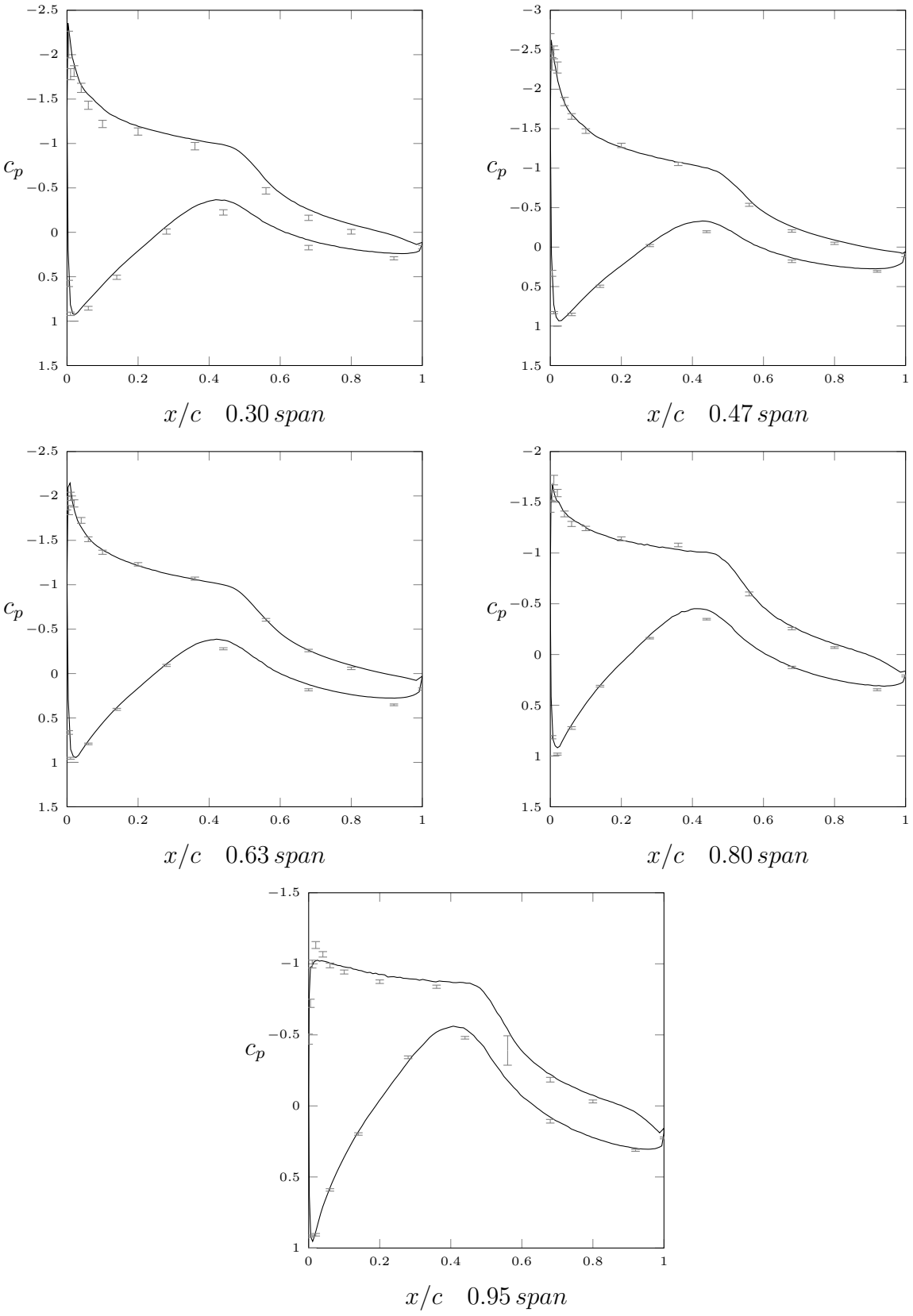

Figure 3.4: *c_p distributions for 7 m/s.*

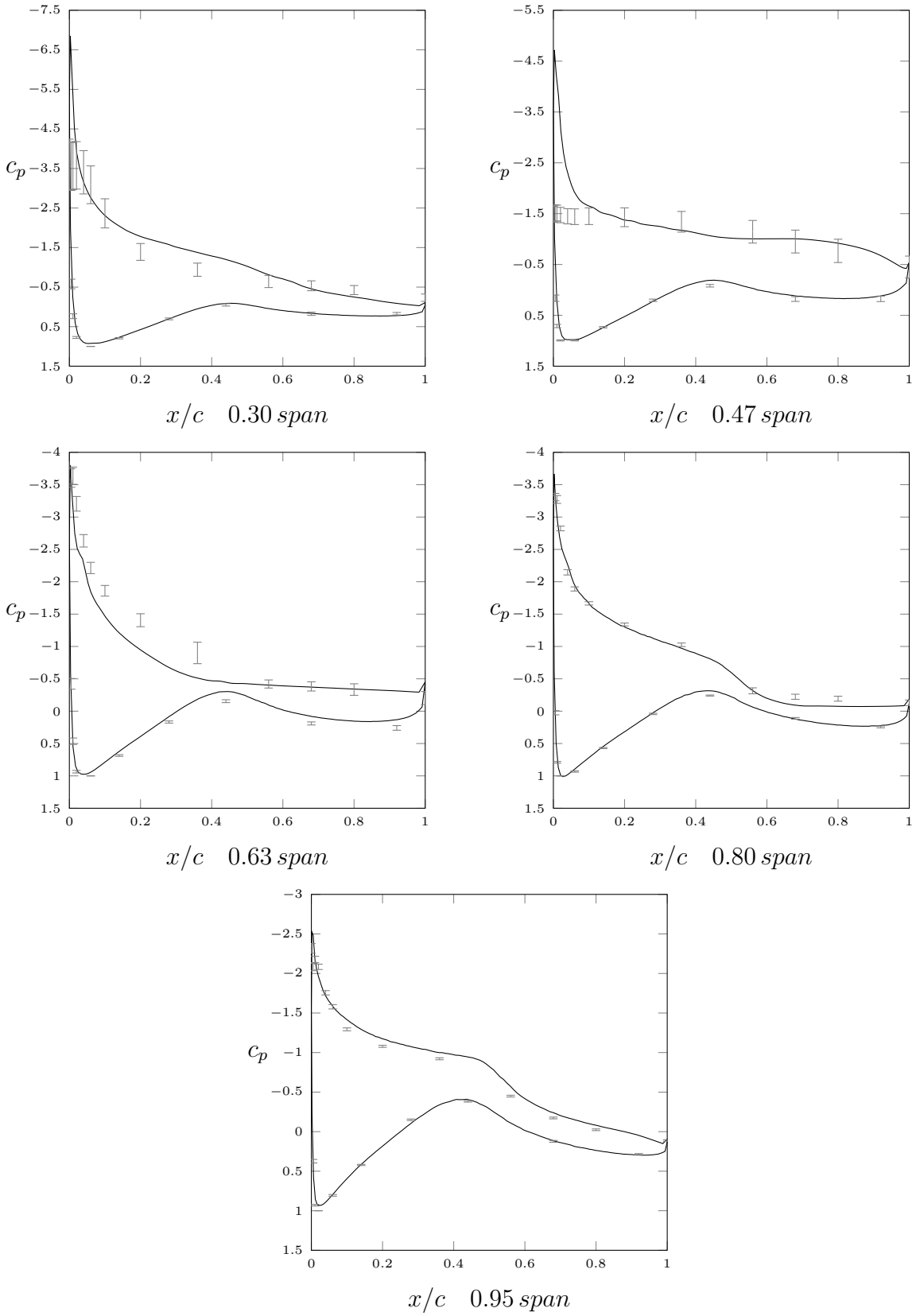

Figure 3.5: *c_p distributions for 10 m/s.*

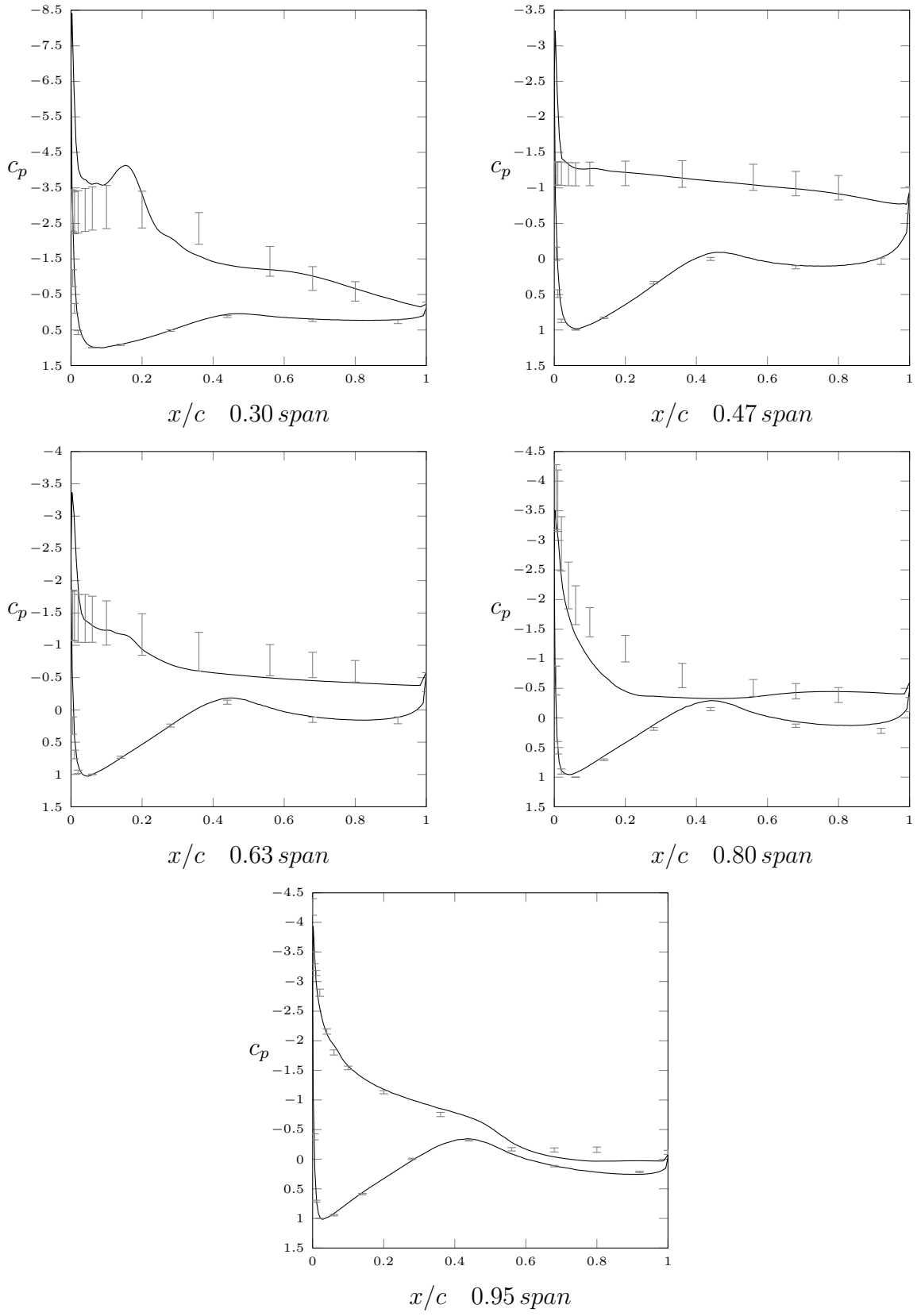

Figure 3.6: *c_p distributions for 13 m/s.*

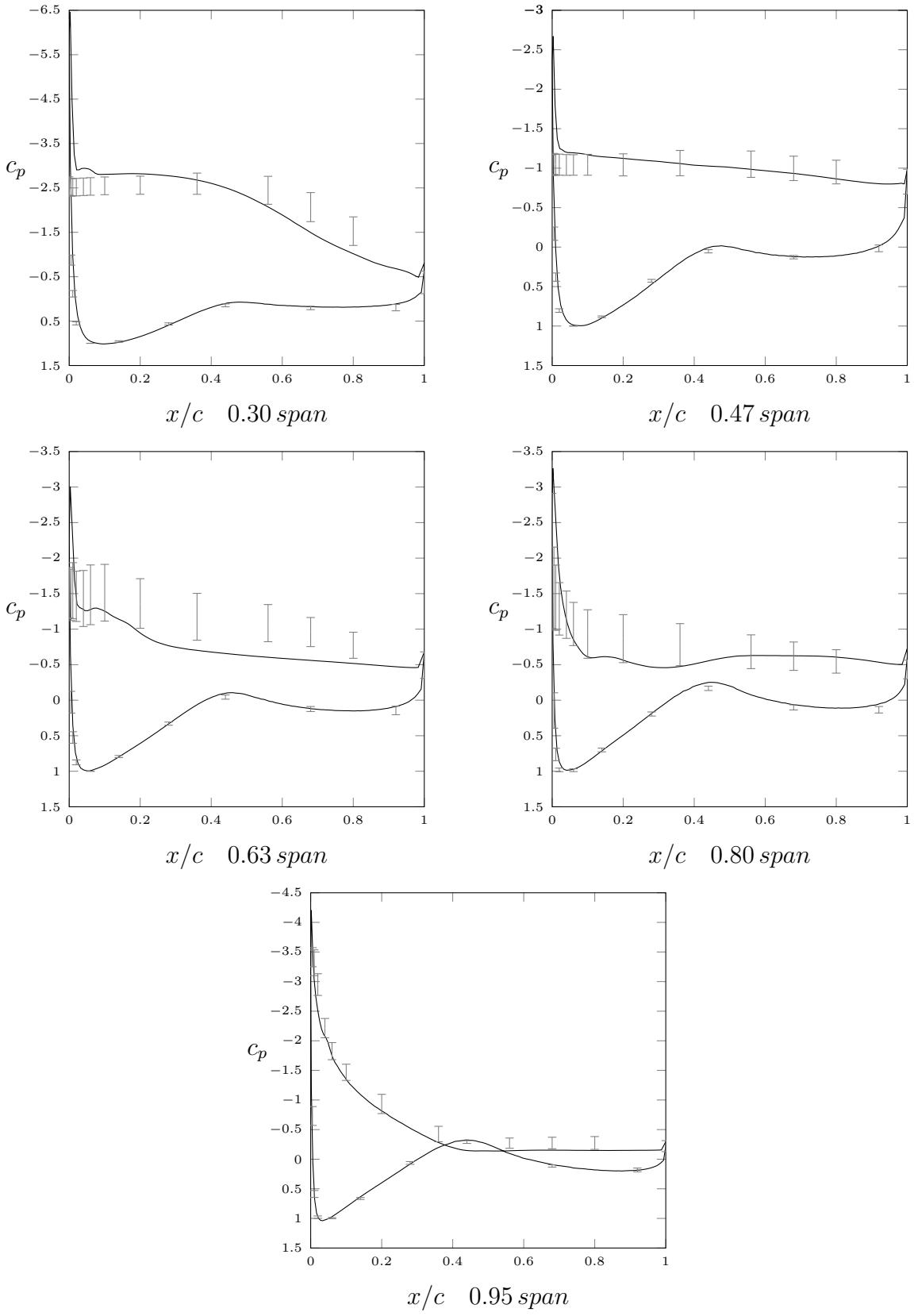

Figure 3.7: *c_p distributions for 15 m/s.*

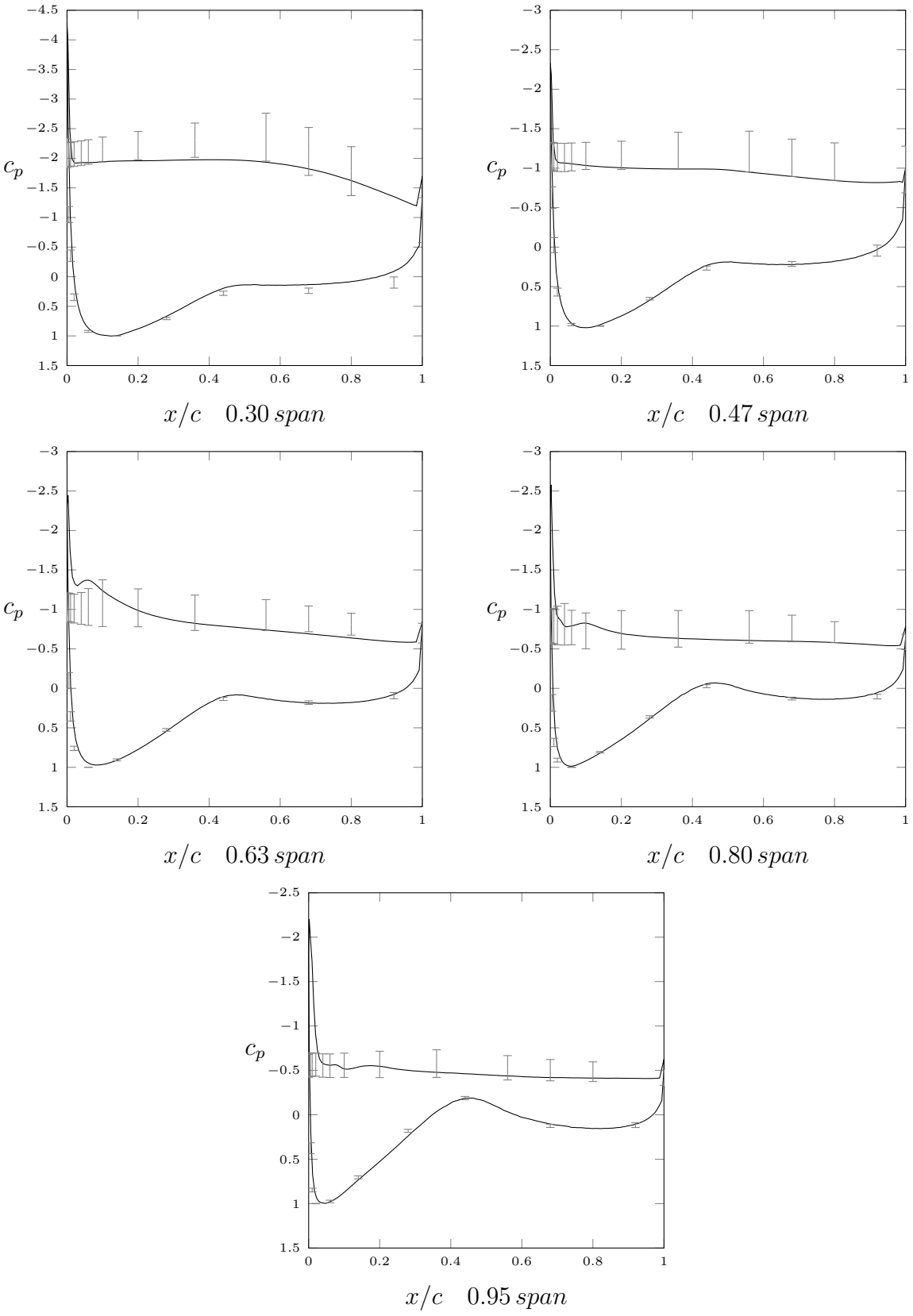

Figure 3.8: *c_p distributions for 20 m/s.*

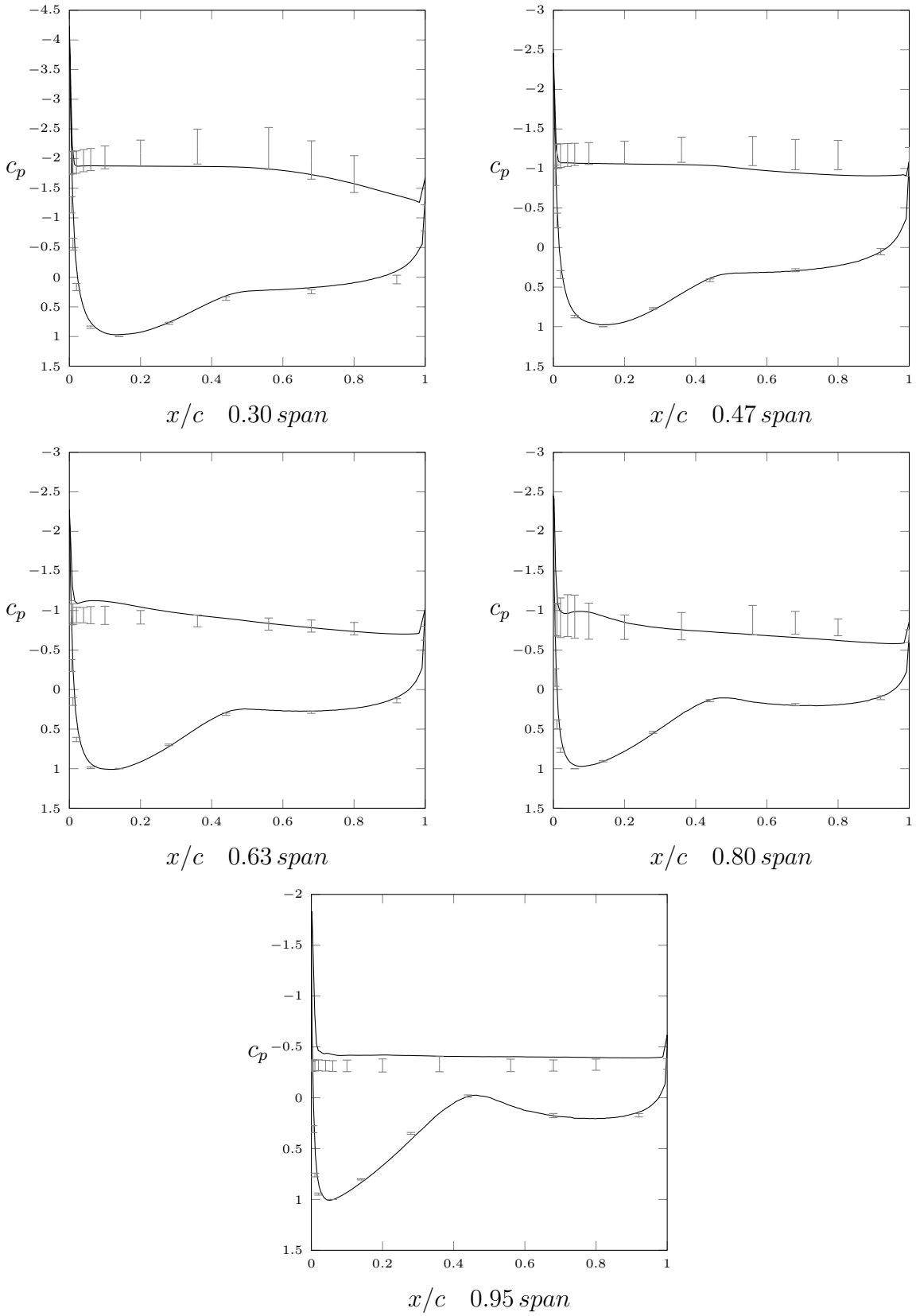

Figure 3.9: *c_p distributions for 25 m/s.*

- 7 m/s: all the spanwise distributions match the measurements, except for 0.30 span, where pressures are slightly underpredicted. The middle zone of the pressure side show a general underpressure for this wind speed. This is also evidenced by the streamlines of Figure 3.3 in the inboard half of the blade for all the spanwise sections. It may be caused by a streamwise vortex which is expected to cause minimal stall effects at 8 m/s for midspan locations [20]. Evidences of stall are detected only in the attachment region. The blade is thus characterized by attached flow, so errors are small in both the sides of the blade. For this reason the low pressure peak is in good agreement with the experimental data.

- 10 m/s: the simulation showed the worst performance in predicting the pressure field for this wind speed. This is probably due to the stall onset, which occurs at midspan around 10 m/s, together with the critical attack angle α values [21]. The 0.30, 0.63 and 0.95 span distributions on the suction side show a little disagreement with the measurements. For 0.30 span the simulated pressure is too low at half chord length, for 0.63 the front part of the suction side shows an overpressure, whereas the high pressures and the 0.95 low pressures are nearly underpredicted. The results are good for all the other spanwise positions instead. The peak is in good accordance on the three last blade stations, but for 0.30 and 0.47 span the modelled pressure is too low.

- 13 m/s: all the CFD results of the pressure side are in good agreement, except for a slight underpressure at 0.80 span. The low pressures follow coherently the measurements for 0.47, 0.63 and 0.95 span. The radial flow begins to influence considerably the c_p distributions. In the suction side of 0.30 span section there is a pressure disturbance around 20% of the chord length, due to the radial air current. The low pressure for 0.80 span section is overpredicted in the front part of the airfoil, and the peak agrees with the measurements for 0.80 and 0.95 span. The stalled sections detect a wrong pressure peak.

- 15 m/s: the stall phenomenon involves now the blade up to 0.80 span and partially 0.95 span. The suction sides of 0.63 and 0.80 span show a slight irregularity compared to the experimental results: in the 0.63 section there is a general overpressure, whereas in the 0.80 section the results are just coherent with the standard deviations. All the other distributions show good agreement, especially for 0.47 and 0.95 span. The pressure peak is correctly modelled only for the last spanwise station.

- 20 m/s: all the numerical results agree well with the measured ones, except a minimum disturbance near the 0.63 span leading edge. The low pressure peaks are a little underpredicted for all the spanwise sections. From this wind speed onwards the blade operates in completely stalled conditions. The incoming air which turns to the suction side after the stagnation point flows in radial direction, limiting the lift generation, and thus the pressure difference at the sides of the blade.

- 25 m/s: the distributions are close to the ones of the previous wind speed. A slight overpressure was found at the ending part of the pressure side for 0.47 and 0.80 span, whereas an underprediction is shown near the leading edge for 0.63 span and along all the suction side for 0.95 span. However, errors are small and a general accordance is confirmed even at the highest wind speed, especially for the pressure side.

From Figure 3.10 and 3.13 the velocity vectors and the corresponding pressure contours of the fluid region around the blade are shown. Two representative cases and span positions are represented, which are 10 and 20 m/s for 0.47 and 0.80 span. The depicted vectors are the tangential projection of the relative velocity vectors, coplanar to the specified span position, and the pressure field is referred to the same plane.

In Figures 3.10 and 3.11 the 0.47 span section is analysed. As previously stated, this radial position experiences stall for 10 m/s, but the flow is still attached at the leading edge. The reversed flow region in fact is limited to the rest of the suction side, resulting in a soft stall development, characteristic of the S809 airfoil. The airflow so flows principally in chordwise direction. The resulting pressure distribution shows a nearly gradual change from pressure side to suction side, except for a slight leading edge pressure peak.

For 20 m/s instead the flow separates abruptly from the entire suction side. A sharp leading edge separation is noticed, as a consequence of the high attack angle α. The rather little reversed current zone of the previous case is replaced by a huge vortex system, which starts from the leading edge and falls back near the trailing edge zone. A severe pressure gradient is also registered between the two sides of the blade, with a wide low pressure zone deeply diffused downwind. The flat pressure field over the suction side is characteristic of the stall behaviour, can be seen also in the plots of pressure distribution.

The situation for 0.80 span is reported in Figures 3.12 and 3.13. The flow attachment on the whole profile for 10 m/s is confirmed for this section, as the stall development involves the inboard and midspan regions of the blade in this case. The acceleration just after the leading edge and the progressive deceleration of the flow over the suction side are represented also by the gradient in the pressure field. Separation is detected for 20 m/s instead, starting from the leading edge. The lower value of α grants a smaller recirculating region if compared to the 0.47 span case. The pressure contour along with the other ones is in accordance with the chordwise distributions explained before.

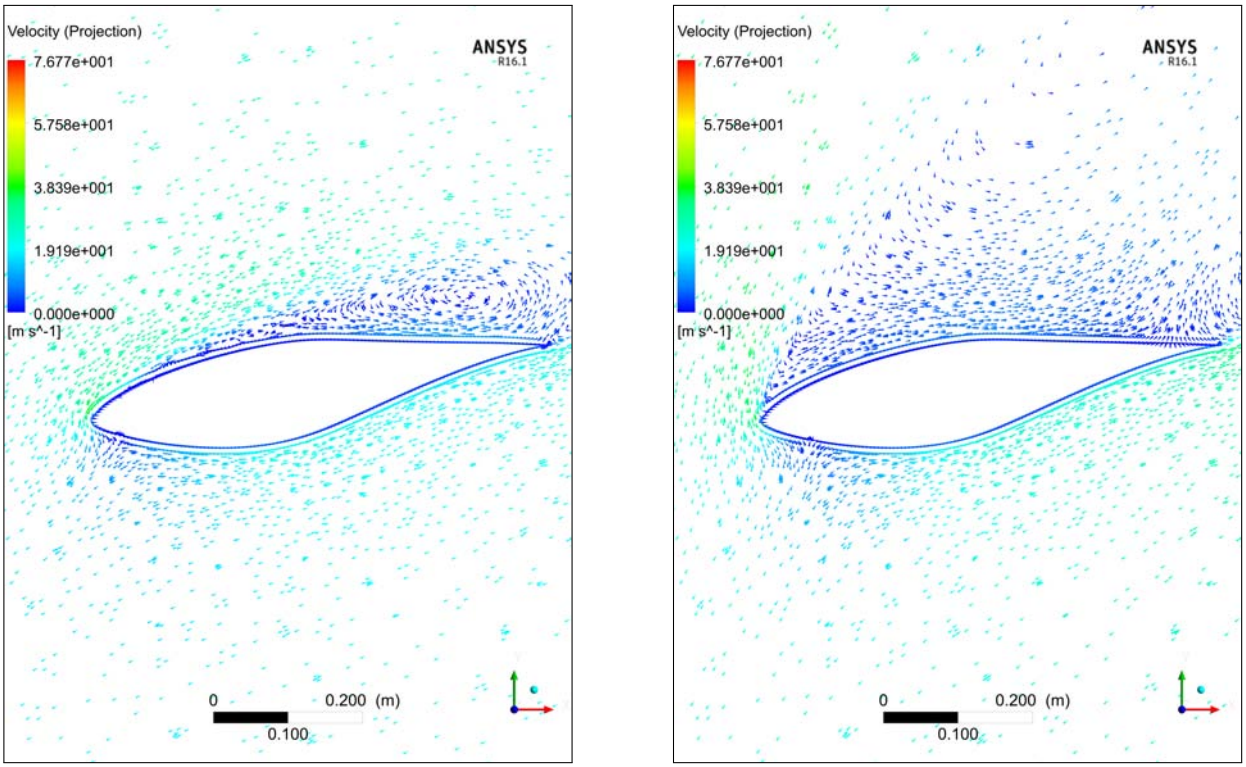

Figure 3.10: *relative velocity vectors for 10 m/s and 20 m/s, 0.47 span projection.*

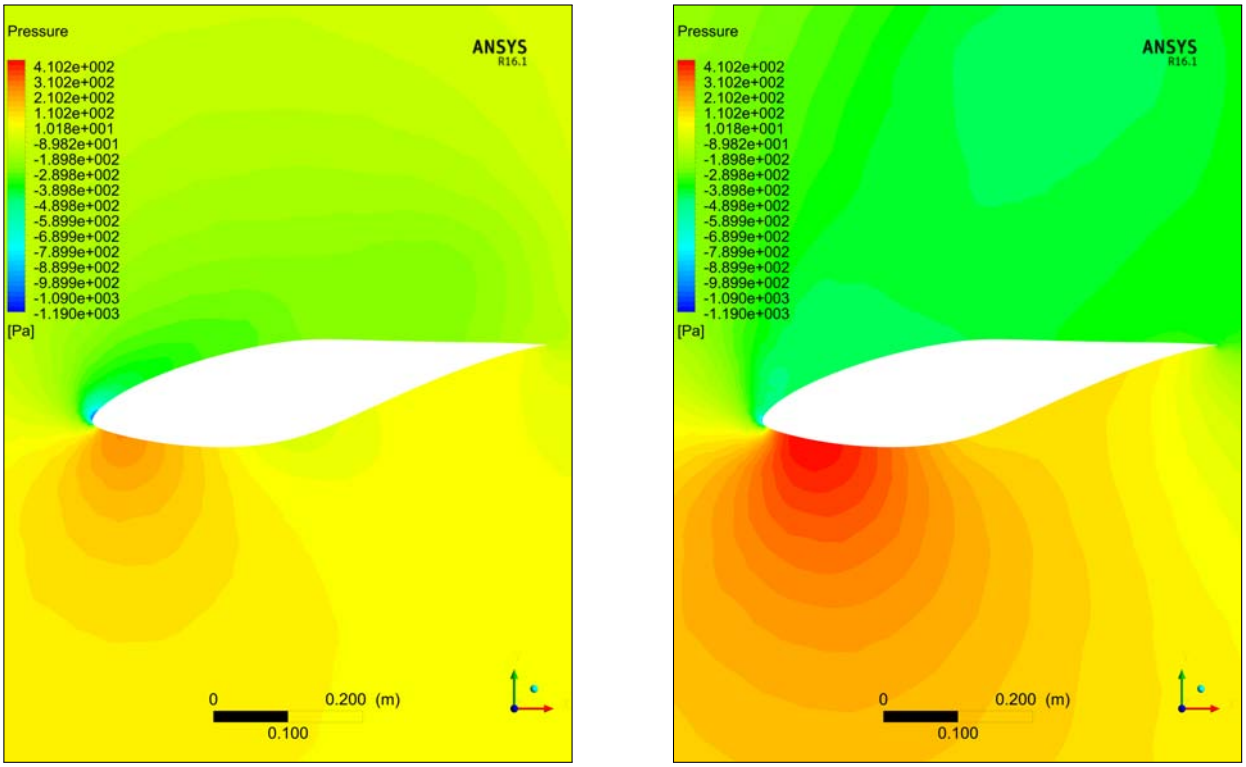

Figure 3.11: *pressure contours for 10 m/s and 20 m/s, 0.47 span projection.*

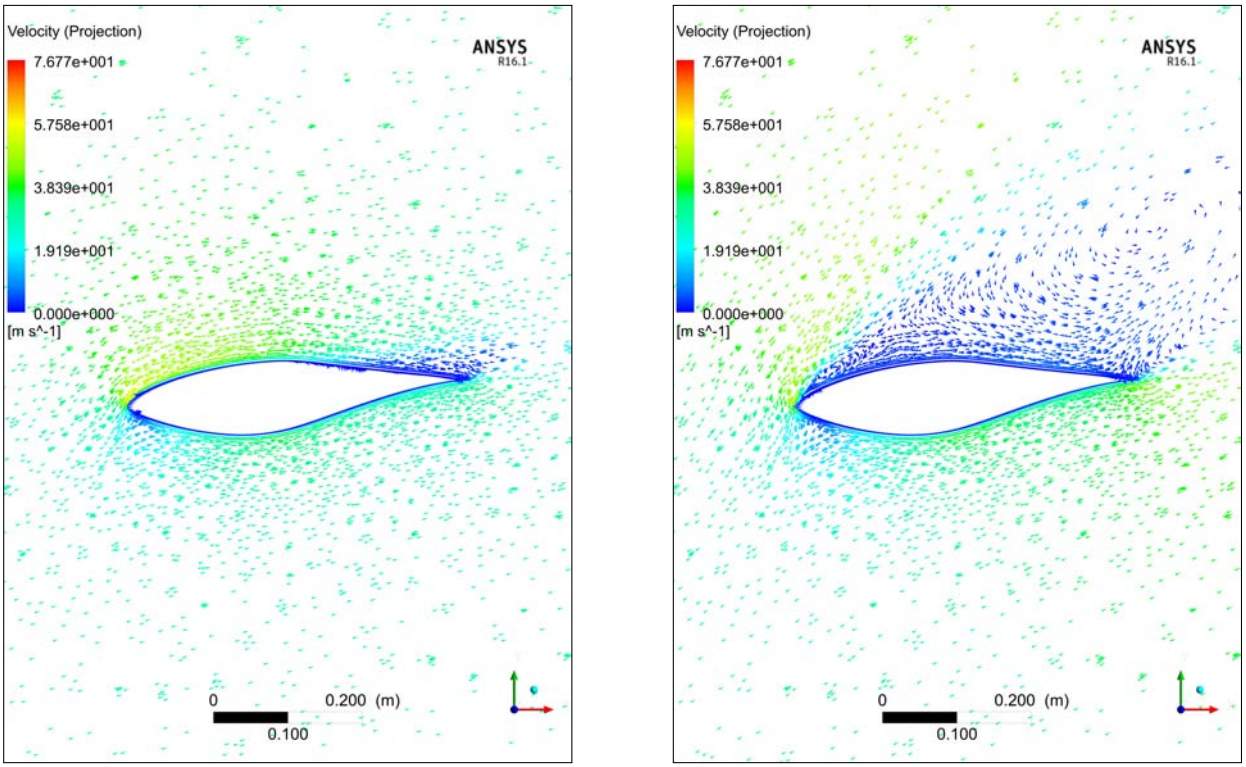

Figure 3.12: *relative velocity vectors for 10 m/s and 20 m/s, 0.80 span projection.*

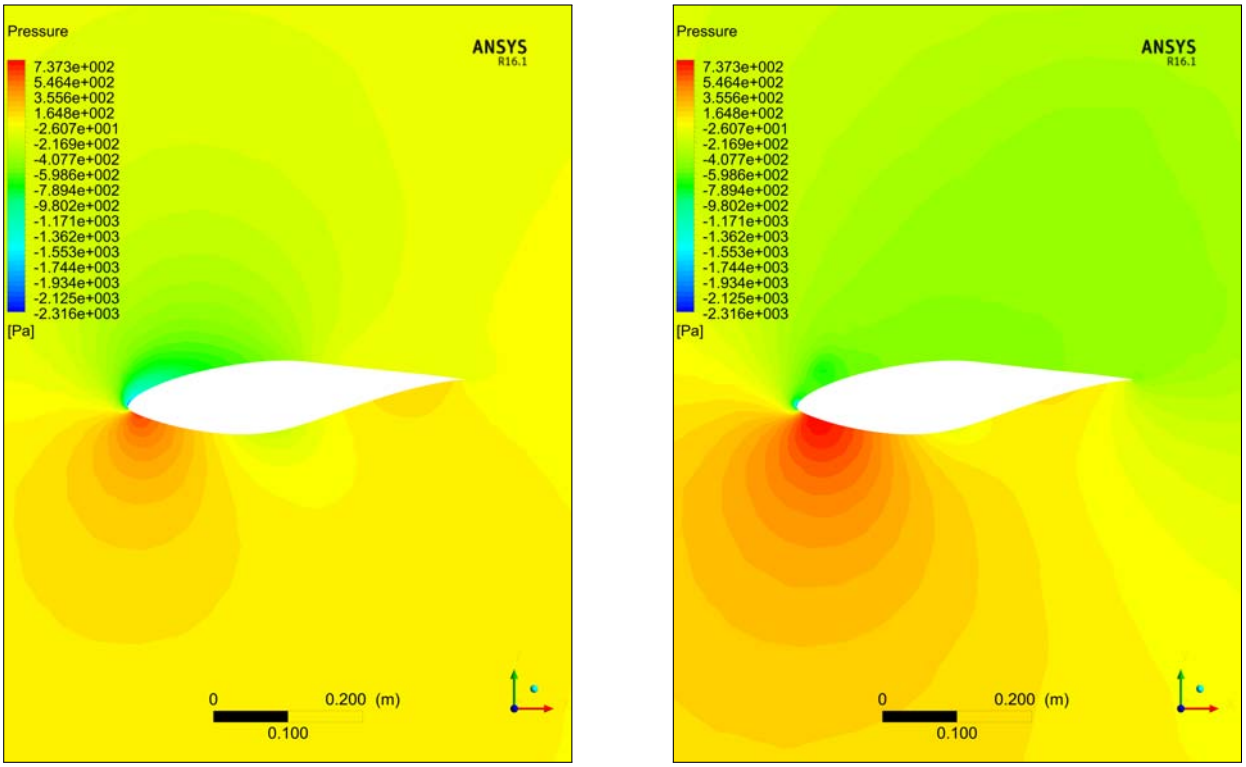

Figure 3.13: *pressure contours for 10 m/s and 20 m/s, 0.80 span projection.*

Torque

The wall forces reports provided the integral value of the aerodynamic torque M_y around y axis for each surface of the blade with the same boundary condition. These values were related to a single blade, so to compute the total effect of two blades the results were doubled. Two moment components are present, a pressure moment due to the lift effect and a viscous moment due to the air friction. The final balance gave the integral value of the aerodynamic torque. During the experiment the low speed shaft torque was measured and then corrected to take in account the gravity effect, which influences in opposite way the down-rotating and the up-rotating blade, in order to take in account only the aerodynamic contributions. In Figure 3.14 the CFD results are reported together with these experimental data for all the wind speeds. The computed torque values show a good agreement with both the overall trend and the standard deviations. The relative error ranges between 1.6 % and 5.7%, with the maximum occurring for 20 m/s.

The peak value is reached for 10 m/s, just before the complete stall growth. For intermediate wind speeds M_y lowers after a brief plateau because of the flow separation even in the outboard blade sections, which are the most important from power production point of view. Anyway the maximum detected and computed torque occurs for the maximum wind speed: the drop gradually stops, followed by a recovery, and for 25 m/s a post-peak is observed. The explanation lies in the radial behaviour of the blade, further discussed. The post-stall operating condition is still not completely understood, due to its strong 3D dependency, but is of utmost importance to grant a reliable design of the whole turbine. In fact, despite the higher power production, the stalled operation is unstable and characterized by remarkable vibrations. For this reason wind tunnel testing together with CFD simulations can help the investigations in this field.

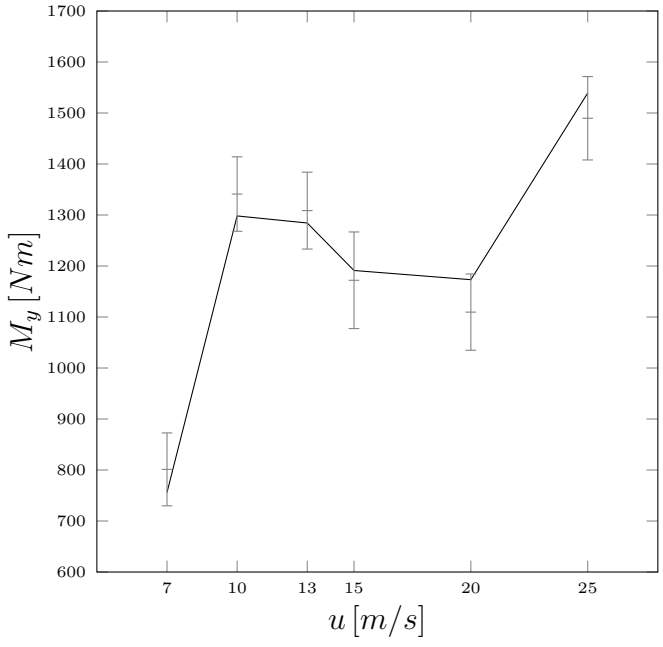

Figure 3.14: *comparison between experimental and calculated aerodynamic torque.*

The integral torque is reference value for the evaluation of the turbine performance. However it's important to separate the global effect from the radial action of the flow on the blade, to understand the 3D behaviour of the process. In Figure 3.15 the radial distribution of the aerodynamic moment $M_y(r)$ along the radius is plotted. The blade divided into sections is shown for an easier interpretation.

- 7 m/s: at this wind speed the moment increases with a linear trend along the spanwise direction, without abrupt changes. This is representative of the attached flow condition, and reflects the pressure results of Figure 3.4. The tip losses become relevant from around 0.90 span, influencing the linear increase of $M_y(r)$.

- 10 m/s: between 0.30 and 0.50 span an enhancement of the moment is registered. This is supposed to be the main contribution to the maximum integral torque value. At this wind speed previous works show that for 0.30 span $\alpha > 20°$, and the maximum lift coefficient C_L is around 2 [22]. Such an increase may be correlated with the formation of a vortex, which reinforces the lift and counterbalances the drag increase in these region [20]. In fact, for relatively high α values, namely for $20° < \alpha < 90°$, the blade behaviour seems to be well represented by the flat plate theory, namely with $C_L \propto \cot(\alpha)$ [23]. All the results are in agreement with these observations. This is strongly related to 3D effects, so more detailed analyses are suggested. Around 0.50 and 0.60 span a drop in the radial moment values coincides with the stall onset. The critical α in fact occurs first at midspan around 10 m/s, as previously stated. For higher span positions the flow is still attached and the moment contribution is noticeable. Around the end of the blade the limiting effect of the tip losses is visible.

- 13 m/s: the stall development enlarges the moment drop in spanwise direction from 0.40 and 0.80 span. However the increase at the radial ends counterbalances the loss at midspan, resulting in a nearly constant torque. The ouboard region of the blade keeps an high moment, because the effect of tip vortices limits the local attack angle and delays stall [23]. The inboard region shows an increased moment for the reasons discussed above.

- 15 m/s: this distribution along the span is very similar to the previous one. The critical stall condition influences more the radial sections around 0.80 span, limiting the resulting moment. This is the power limitation due to the stall-regulation of the turbine. The tip region is not completely stalled yet, thus a moment contribution is registered, as in the 13 m/s case.

- 20 m/s: hereafter the blade operates in stalled condition. The torque value is nearly equal to the 15 m/s one. In fact the increasing moment between 0.30 and 0.40 span is clearly visible. In these regions C_L decreases only slightly within the studied range of wind speeds, then the torque is enhanced even in stalled conditions.

- 25 m/s: the effect noticed for the previous wind speed influences even the midspan region. Assuming the flat plate theory becomes valid with increasing α, a high C_L is maintained. Together with an higher wind speed, this leads to the post-stall peak in the integral torque.

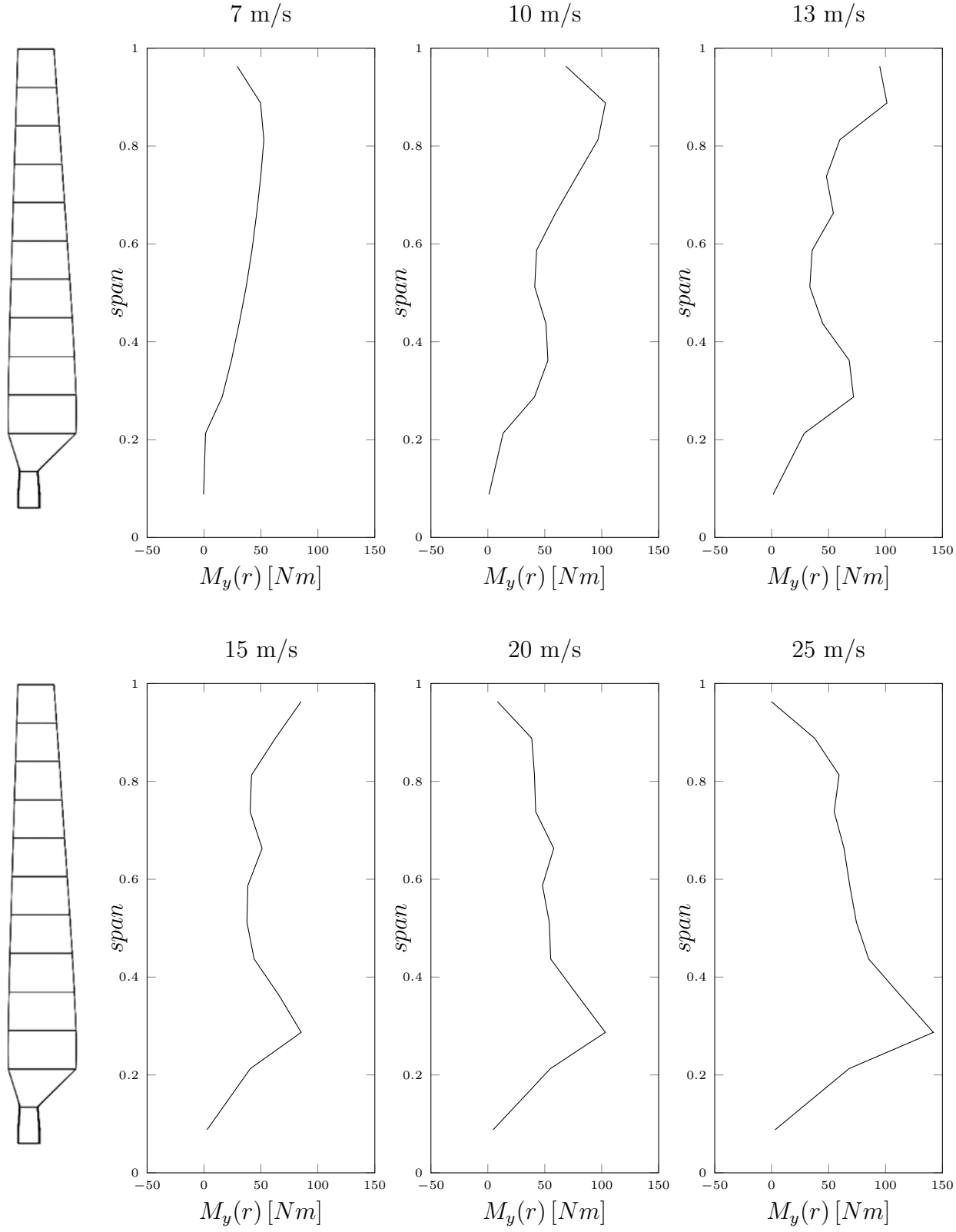

Figure 3.15: *aerodynamic moment varying in spanwise direction for all the wind speeds.*

- IV -

Wind gusts

After the steady model validation, the second part of this thesis begins with a review on the general definitions and properties of strong and sudden wind events, namely wind gusts. Physical explanations, detection techniques and proper modelling are proposed, to provide a background before going deeper with the unsteady CFD analysis of the next chapter.

Overview

The technological advancement in wind turbines is not only centred in a higher energy efficiency, but also in a more safe and economical design of the machine. From this point of view, a deeper knowledge of the environmental conditions in which the turbine has to operate is of utmost importance. Hence methods for the prediction and simulation of a possible extreme load event have been developed.

A wind gust is defined as a short term speed variation within a turbulent wind field. Its typical shape can be characterized by some parameters, as clarified in Figure 4.1 [3]. The flow field, incoming with an average speed $\overline{u}$, is followed by a negative fluctuation, a positive peak and another negative pulse before stabilizing again. The gust relative amplitude a is the speed difference $\overline{u} - u_{max}$. The gust rise time b is defined as the period between the beginning of the gust and the reaching of the maximum speed u_{max}, whereas the maximum gust variation c is the absolute difference $u_{max} - u_{min}$. The lapse time d is defined as the period between the maximum and minimum velocity occurrences. A parameter to evaluate the gust magnitude is the gust factor $G = u_{max}/\overline{u}$.

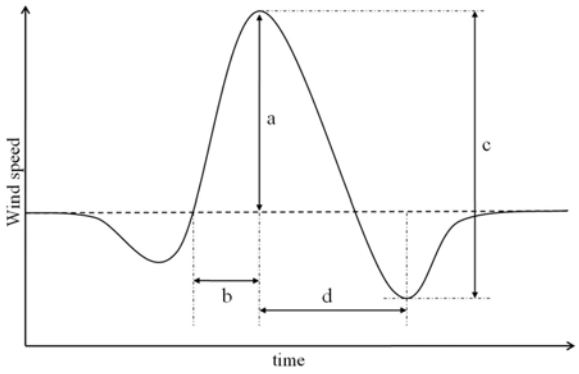

Figure 4.1: *characteristic parameters of an average wind gust* [3].

Atmospheric Boundary Layer

The lowest portion of the atmosphere, where the wind turbine is likely to operate, is called Atmospheric Boundary Layer (ABL) and ranges approximatively between 0 and 2000 m. Its behaviour is important for the turbine productivity and preservation. Some factors have to be considered to characterize the ABL, such as atmospheric turbulence and local wind conditions. Atmospheric turbulence is governed by two main mechanisms, as explained below.

- *Mechanical*: at any altitude z_i, wind velocity is greater for $z > z_i$ and lower for $z < z_i$. Ground roughness in fact casue this frictional loss. This lack of equilibrium of forces amplifies the disturbance of turbulence, tending to curl the shear layer into vortices. The most popular methods to define the dependency of velocity with height are the log law and power law. Log law is expressed by Equation 4.1, where $\kappa \sim 0.4$ is the Von Kàrmàn constant and z_0 the surface roughness length. Nevertheless this definition corresponds to the traditional logarithmic velocity profile of a wall-bounded turbulent fluid flow with no-slip condition [15]. Equation 4.2 represents the power law instead, with z_r and $u(z_r)$ respectively a reference height and the consequent wind speed. The first model is based on roughness data, whereas the second does not need such informations. The exponent α depends on many parameters, namely elevation, time of the day and of the year, terrain, wind speed and temperature. Empirical relations exist, but for a neutral atmosphere condition[1] with no obstacles it is approximatively equal to 1/7. If structures or trees impede the near-surface wind, the log law is suggested.

- *Thermal*: with the increasing altitude, air experiences also a variation of temperature. The lapse rate is defined as the rate at which atmospheric temperature decreases with z. For a standard ABL, it is equal to -6.5 $\cdot e^{-3}$ $°C/m$. However great variation may occur for different sites and atmospheric conditions. Anyway, a temperature difference is present, so natural convection is expected. The convective effect due the rising of hot air and the consequent heat fluxes provide more turbulent kinetic energy. Thus atmospheric turbulence and mixing are enhanced.

$$u(z) = \frac{u^*}{\kappa} \ln\left(\frac{z}{z_0}\right) \tag{4.1}$$

$$u(z) = u(z_r)\left(\frac{z}{z_r}\right)^{\alpha} \tag{4.2}$$

[1] A neutral atmosphere condition stands when the potential temperature Θ is constant with altitude, or $d\Theta/dz = 0$. The potential temperature, defined as $\Theta = T(p_0/p)^{R/c_p}$, is the air temperature resulting from an adiabatic process from p to reference p_0, in order to evaluate the temperature difference based only to the different heat content, so without the compressibility contribution.

Local wind conditions are caused by pressure differences in the air layer. From the moment that different zones experience different solar radiation, a thermal imbalance is created. Hence air fluxes are moved, also under the effect of Coriolis forces. Different time and spatial scales exist for these air motions. Both the scales become of interest for a single wind turbine at their minimum values: small-scale wind circulations, caused by topological variations which determine the ABL structure, within short time scales of minutes and seconds. This is the domain of wind gusts. In particular, the relevant fluctuations regarding wind turbines are between 1 and 100 m in periods of 1 s to 10 minutes. Hence a rather high sampling frequency of 1 - 5 Hz is necessary for an appropriate gust measurement.

Gust detection

Criteria exist for the evaluation of the extreme wind conditions in a given site, according to wind measurements from historical databases or performed on purpose. After a wind data set has been acquired, a computational algorithm can be employed to characterize wind gusts from the rest of the fluctuating signal. If a wind gust is treated as a stochastic process, its characteristic time τ_G is defined as the period in which the autocorrelation function satisfies $0.75 < \mathrm{ACF}(\tau_G) < 1$, therefore when turbulent fluctuations remain almost correlated [24]. The principal detection procedures are summarized below.

- *Peak to peak*: a time step of τ_G size is defined and moved through the time series. At the time t the local difference $u_{max} - u_{min}$ is evaluated, referring to the speed values between t and $t + \tau_G$. After the complete dataset has been scanned, the maximum difference is taken as the extreme gust over the sample. This method is suitable for detecting sudden variations, but only the maximum one is considered.

- *Velocity increment*: again a moving time step is used, but only the first and the last velocity within τ_G are considered, and the difference $u(t+\tau_G)-u(t)$ is evaluated. The step where this difference is maximum is taken as the extreme gust. The procedure is faster and requires less computational cost, due to the less data treated at each step. However, steeper fluctuations are not detected.

- *Peak over threshold*: the definition of an absolute amplitude threshold A_G and a minimum event duration d_{min}, in which the condition $u > A_G$ has to be satisfied, allow to filter the small scale fluctuations. A maximum duration d_{max} can also be set, so that if the previous condition is fulfilled for a longer period, the gust detection is excluded. There is neither dependency on τ_G nor on the moving time step, and the method is good for cases where only the extreme peak values are of interest. Sudden variations are not taken in account, and other methods may assist this deficiency if dynamic loading is of importance. This is one of the most employed technique.

- *Acceleration over threshold*: this is an extended version of the previous method. In fact an additional acceleration criterion is introduced. A fluctuation is detected as a gust if the difference $u(t) - u(t - \tau_G)$ divided by the characteristic time τ_G overcomes a specified acceleration limit. Here the instant t indicates the moment when the wind speed overcomes A_G. Dynamic loading characteristics and fast variations are detected, but the method is rather arbitrary and may not point out some gusts due to the values choice for the involved parameters.

Gust models

The importance of gusts for structural issues and loading assessments, combined with their inherent random nature, promoted the development of various gust models. Average gust shapes, probability distributions and simulated wind fields were investigated. The simplest gust models derive from plain mathematical functions. These are Gaussian profiles or sinusoidal profiles, as one-minus-cosine, sine and cosine [25]. The one-minus-cosine is one of the most popular average gust shape model, due to its simplicity, and is currently adopted for load assessment in aerospace industry and international standards. However a good matching with experimental gust measurements is not always present.

Therefore more complex descriptions were investigated. Many approaches are based on the statistical approach of averaging a suitably large number of measured gusts to define a gust shape model. Larsen et al. [26] discuss a model to extract a mean speed gust shape based on the peak over threshold detection procedure. The benefit of including a realistic gusts in the stochastic turbulence of ABL is explained. The original stochastic time series is transformed into a series of Dirac delta functions located at the detected gusts intervals, more precisely at the peak instant. The mean gust shape is then extracted as a function of ACF, turbulence standard deviation, gust amplitude and time. The spatial shape of the gust is investigated too, by applying the previous procedure also to a second position. The produced gust shapes are then compared both with measured wind datasets and numerically simulated wind field, with good results. Various terrain conditions and atmospheric stability situations are tested too.

The avaiability of useful measurements for the gust assessment is limited in space and time though. Knigge and Raasch [27] performed a LES simulations to provide a virtual multi-dimensional datasets of atmospheric turbulence with all the ABL characteristics. Both 1D and 2D gust profiles were extracted by means of peak over threshold method. A comparison between the obtained 1D gust profile, the one-cosine gust shape and the measured data is performed. A noticeable difference is found between the 1D profile from LES calculation and the one-cosine shape, mostly in the steep increase and decrease of the wind speed. Therefore an adjustment is proposed for the one-cosine formulation, parametric for each component of the velocity vector. The accuracy of the method is underlined for low altitudes, suitable for wind turbine applications.

Seregina et al. [28] demonstrate the extrapolation of wind gust velocities from common hourly measurements. The hypothesis made is that both wind and gust velocities follow Weibull distributions. Then the gust model is build as a transfer function between shape and scale parameters of the two different distributions. As gust are fluctuations of wind, the two distributions are thought to have similar shape and different scale. Therefore the estimation of the gust speed by the combination of the two Weibull functions is explained and validated with meteorological data.

Mann [29] elaborated an algorithm to simulate a complete 3D turbulent wind field with realistic ABL behaviour, including gusts and shear layer. The model is based on the spectral tensor for atmospheric turbulence at high wind speeds. The wind turbine company Vestas developed an appropriate software which generates a wind field based on Mann model and gives a 3D velocity components as output. The field is divergence-free, so mass is conserved and the use in CFD simulations is possible.

IEC STANDARD

Besides the deep resarch about wind gusts, the urgency of a safe turbine operation claims for straighforward specifications. As other works about wind turbines and gusts, the approach adopted in this analysis follows the International Electrotechnical Commission (IEC) guidelines [30] - [32]. A series of well-defined wind gust models with a set of extreme loading cases are listed in IEC 61400-2 [33][2]. Even if the standard is meant for design purposes, in the present work it has been used as an international reference for the definition of a gust shape and for an immediate structural verification. For these reasons the cases analysed in Chapter 5 don't follow exactly the load cases of the standard, as the main goal is to study the aerodynamic response of the turbine in a transient operating condition.

Larger machines are provided with control systems to prevent rotor overspeed and blade overload, but the turbine has to withstand even these loads for safety and continuity reasons. In fact, a system fault is always possible. The most commonly followed procedure consists in the definition of several load cases which may represent the turbine lifetime. The critical loads can be divided in ultimate and fatigue loads. In this analysis, a numerical ultimate check is performed for a EOG (Extreme Operating Gust) with a recurrence period of one year, as discussed in the next chapter.

Wind profiles

The external wind conditions specified in IEC 61400-2 are now explained. The normal wind profile is based on the power law of Equation 4.2, with $z_r = z_{hub}$ and $\alpha = 0.2$. This is the steady wind profile that the turbine is supposed to deal with in standard conditions. Then the extreme steady wind conditions are consequently defined with a similar profile, considering recurrence periods N of one or 50 years. This period means how often the particular event is likely to happen. Therefore Equation 4.3 and 4.4 express the extreme wind profiles, respectively for $N = 50$ and $N = 1$. These conditions are based on the reference speed u_{ref}, which is the 10 minutes average wind speed at hub height for $N = 50$. It is a basic parameter, useful also to distinguish four SWT classes accordingly to wind speed and turbulence ranges. All the velocity profiles defined until now are constant with time.

$$u_{e50}(z) = 1.5\, u_{ref} \left(\frac{z}{z_{hub}}\right)^{0.11} \tag{4.3}$$

$$u_{e1}(z) = 0.75\, u_{e1}(z) \tag{4.4}$$

[2]The cited standard refers specifically to Small Wind Turbines (SWT), with a swept area and generated voltage up to 200 m^2 and 1 kV AC / 1.5 kV DC For larger rotors, IEC 61400-1 has to be considered.

Once defined the steady extreme profiles, a series of severe transient events which the wind turbine should withstand during its lifetime are explained. These conditions are defined as a varying average profile superimposed over a mean flow. Depending on amplitude, shape and duration, four wind gust models are proposed in the standard.

- *Extreme Operating Gust* (EOG): this is the most representative gust profile, a symmetric Mexican hat shape. Before and after the rather steep peak, a brief speed dip is included. Gust amplitude and duration vary with the return period. The analytical form is expressed by Equation 4.5, for $z_{hub} < 30\ m$, and the resulting velocity fluctuation at hub height in time is reported in Figure 4.2. A normal stationary profile $u(z)$ is supposed to persist up to $t = 0\ s$, when the gust begins. The variables involved are further explained. Equation 4.6 gives V_{gustN}, the hub height gust magnitude with a recurrence period of N years. The parameter β is equal to 4.8 for $N = 1$ and 6.4 for $N = 50$, and D is the rotor diameter. The gust period T is the total event duration, considered 10.5 s for $N = 1$ and 14 s for $N = 50$. After that time, the velocity profile goes back to $u(z)$. Hence the EOG vertical profile shape in time corresponds to a pulsating normal profile.

$$u(z,t) = \begin{cases} u(z) & t < 0 \\ u(z) - 0.37\, u_{gustN}(z)\, sin\left(3\pi\frac{t}{T}\right)\left(1 - cos\left(2\pi\frac{t}{T}\right)\right) & 0 \leq t \leq T \\ u(z) & t > T \end{cases} \tag{4.5}$$

$$u_{gustN}(z,t) = 0.18\,\beta\,\left(\frac{2}{3}u_{hub} + 5\right)\left(\frac{1}{1 + 0.1\frac{D}{0.7z_{hub}}}\right) \tag{4.6}$$

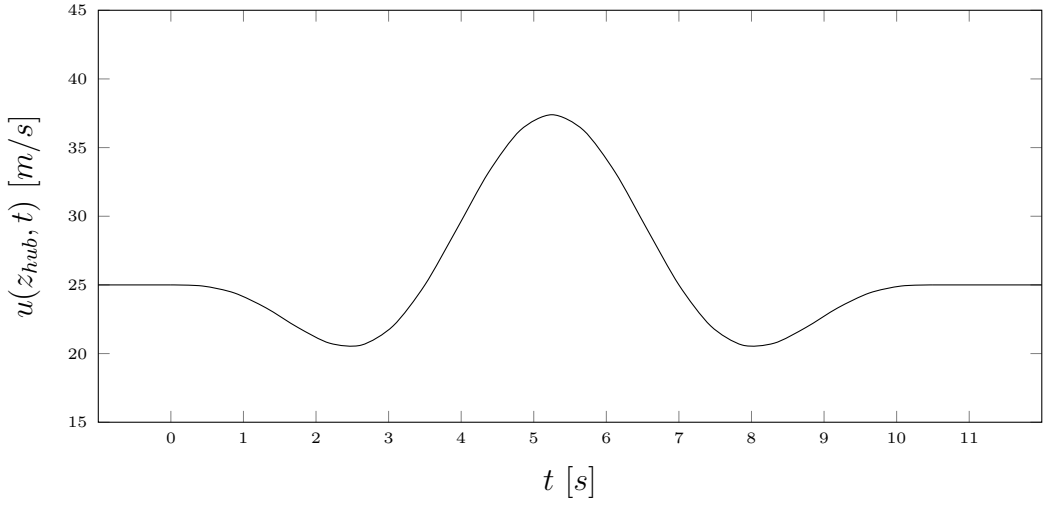

Figure 4.2: *EOG profile for $N = 1$ and $z = z_{hub} = 12.2\ m$* [33].

- *Extreme direction change* (EDC): a sustained change in the angle of wind direction is defined by Equation 4.7 as a one-cosine-shaped profile $\theta_N(z,t)$. Its amplitude varies with N, and the transition time T is equal to 6 s. The term θ_{eN} is the direction change magnitude, which can be expressed in a compact form by Equation 4.8 as function of the previously defined extreme gust magnitude, and has to be considered either with positive or negative sign according to the resulting worst loading condition.

$$\theta_N(z,t) = \begin{cases} 0 & t < 0 \\ 0.5\,\theta_{eN}\left(1 - \cos\left(\pi \frac{t}{T}\right)\right) & 0 \leq t \leq T \\ \theta_{eN} & t > T \end{cases} \tag{4.7}$$

$$\theta_{eN} = \pm\beta \arctan\left(\frac{u_{gustN}(z)}{\beta\, u_{hub}}\right) \tag{4.8}$$

- *Extreme Coherent Gust* (ECG): in a similar way as EDC, a sustained change in wind speed magnitude is defined by Equation 4.9, imposed as a one-cosine shape. Gust amplitude and duration depend on N, and the coherent gust magnitude u_{cg} is set to 15 m/s, whereas the gust rise time is $T = 10$ s.

$$u(z,t) = \begin{cases} u(z) & t < 0 \\ u(z) + 0.5\,u_{cg}\left(1 - \cos\left(\pi \frac{t}{T}\right)\right) & 0 \leq t \leq T \\ u(z) + u_{cg} & t > T \end{cases} \tag{4.9}$$

- *Extrene Coherent Gust with Direction Change* (ECD): this gust shape is obtained from the combination of the previous two models. The rise of wind occurs simultaneously with the direction change.

Load cases

The wind profiles discussed above are matched with the possible machine states to obtain several operative conditions. The life of the STW is therefore represented as a set of design situations covering the most significant events which the turbine may experience. Hence four groups of load cases are proposed.

- *Operative load without fault*: this is the most common case. An operative load is defined for the turbine in its normal productive operation. The suggested wind conditions to be tested are ECG and EOG.

- *Operative load with fault*: the occurrence of fault is supposed to be not correlated with an extreme wind event, so a normal wind profile is considered for this set of load cases. If an external fault occurs, such as the loss of grid connection, no resistance would be met by the aerodynamic torque, so the rotational speed would increase until the brake system is brought into action. A possible correlation between an extreme wind event as EOG and a grid fault event is considered.

- *Non-operative load without fault*: a non-operative load is defined when the turbine is parked or idling, namely in safely stopped position or rotating at its minimum speed. The external condition proposed is the EOG.

- *Non-operative load with fault*: in these cases the possible failure of yaw or pitch mechanisms is suggested to be evaluated together with a EOG wind condition. In other words the turbine may be parked with a dangerous angle with the incoming extreme wind.

The load values can be achieved from a simplified calculation method included in the standard, from aeroelastic models or from load measurements and extrapolation. In this study the following source of loading are treated:

- *Aerodynamic loads*: these loads arise from the interaction between the airflow and the blades at different radial distances. Thus they increase approximatively linearly with radius until the tip losses become relevant, as demonstrated in Chapter 3.

- *Gravitational loads*: gravity acts with constant direction, so the resulting load depends on azimuth angle γ. It may be a pure compressive ($\gamma = 0°$) or tensile ($\gamma = 180°$) loading, a pure bending moment ($\gamma = \pm 90°$), or a combination of the previous.

- *Centrifugal loads*: unlike the previous loads, this is a constant value depending only on rotational speed, blade mass and radius.

Stress calculation

The action of the individual loads as moments and forces has to be translated into stresses to verify the turbine structural integrity. The stresses acting at the blade root are analysed in Chapter 5. Axial stresses and bending stresses were calculated using the IEC Equations 4.10 and 4.11 for a circular blade root. F_z is the axial force, A the blade root section, M_{xx} and M_{yy} the bending moments around x and y axes, whereas W is the flexural section modulus. These stresses shall be combined to find the equivalent one, which has to be then compared with the material ultimate strength σ_U as shown in Equation 4.12. The coefficients γ_L and γ_M are the partial safety factors for load measurements and material properties, depending on the uncertainties involved in their determination, as explained in the standard.

$$\sigma_z = \frac{F_z}{A} \tag{4.10}$$

$$\sigma_M = \frac{\sqrt{M_{xx}^2 + M_{yy}^2}}{W} \tag{4.11}$$

$$\sigma_{eq} = \sigma_z + \sigma_M \leq \frac{\sigma_U}{\gamma_L \gamma_M} \tag{4.12}$$

- V -

Unsteady CFD investigation

The last chapter focuses on the aerodynamic response of the Phase VI turbine within an extreme and unsteady load event. Two configurations are numerically investigated, namely operational and parked positions. The moving mesh approach is presented with all the solver settings. Results regarding loads, pressures and streamlines are then discussed.

General settings

Configurations

Unlike the CFD validation performed in steady-state conditions, for the transient simulations the time derivative of Navier-Stokes Equation 1.4 is introduced. Once defined the IEC 61400-2 extreme wind events, as explained in the previous chapter, two simulations in different machine setups are here analysed. These configurations are inspired to the load cases 2.2, 2.3 and 5.1 of the standard. The main difference though is that the analysis is principally meant for aerodynamic response analysis, and not for design purposes. The two cases can be summarized as follows:

- *Operative case*: the extreme wind event selected is the EOG with $N = 1$. During the gust the turbine was kept in its normal operation to allow the analysis of the blade response in terms of aerodynamic torque M_y and stresses at the root section.
- *Parked case*: the same EOG was imposed to the parked turbine. This *Phase VI* configuration is obtained by the simultaneous feathering of the two blades, in order to put the tip chord parallel to the incoming wind, so with a tip pitch of 90°. The two blades are located at $\gamma = 0°$ and $\gamma = 180°$ azimuth angles. The lift effect is minimized, therefore this corresponds to the safety turbine position. The goal is to demonstrate the benefit of this operation for such high wind speeds.

In Figure 5.1 the two turbine configurations are represented. Moreover neither in the official NREL report nor in other works indications are included for the cut-out wind speed u_{co} [6]. A value of 25 m/s can be suggested from literature, but a more general approach is here proposed. In the operative case, u_{co} is supposed to be higher than the maximum gustspeed, whereas in the parked case u_{co} is thought to be 25 m/s. Alternatively, the first configuration can be considered as characterized by a faulty pitch system. For passively controlled turbines, as stall-regulated turbines, this is a potential machine fault [33].

Firstly, the mesh of the entire rotor was obtained by copying the validated mesh, pasting and rotating it around the y axis. The front view of the control volume cross-section is visible in Figure 5.2. The inner and outer domains became respectively a cylinder containing the two bladed rotor, and a cylinder with a hollow region. The periodic conditions for the middle mesh were cancelled. Boundary settings for the surface meshes of the inner domain and of cavity of the outer domain were initialized in Pointwise as *interface*. Furthermore these two cylindrical surfaces were split in front, rear and lateral surface conditions, for a total of 6 surface conditions. This procedure is necessary to make these interfaces selectable in Fluent, as further explained.

Also the parked turbine model was obtained from the validated half-rotor mesh. In Pointwise the inner volume mesh was deleted, together with the surface mesh and boundary layer of the cylindrical blade attachment, otherwise the rotation of the next step would result in a wrapped and self-intersecting mesh. The remaining part of the meshed blade was selected and the *rotate* transformation was engaged, and an angle of 87° was imposed. Therefore the tip section resulted aligned to the free stream wind velocity, with the leading edge pointing upwind. The surface mesh and the boundary layer of the hub attachment were created again, and the inner domain too. After that, the entire mesh was doubled as previously done. No mesh interfaces had to be set, since this is a stationary case. The two computational grids are obviously different, but they are both composed of 8.5 million elements.

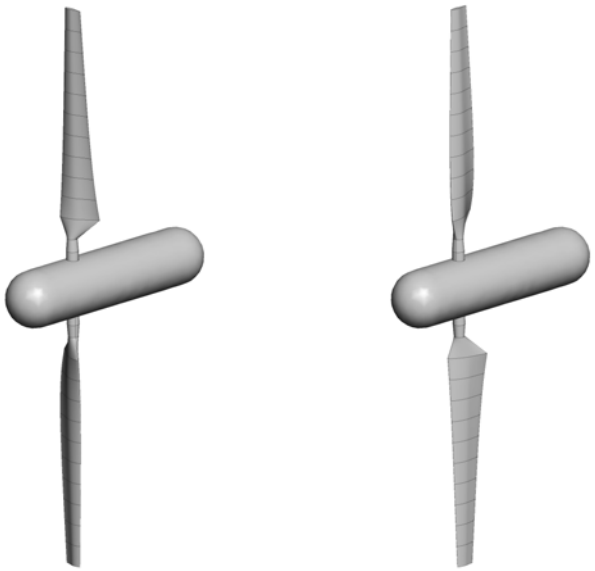

Figure 5.1: *turbine rotor with regular pitch and feathered blades.*

Moving mesh

In ANSYS Fluent, the moving mesh, or sliding mesh strategy, is a particular case of the dynamic mesh motion, which allows to move specified cell zones and to modify the mesh consequently, either rigidly or dynamically [18]. In this case, the rigid movement is considered. To allow such movement, interface surfaces have to be defined to connect different cell zones. If a mesh zone moves, its interfaces and are accordingly updated to define the new position for the linked zones. If the interfaces remain in contact fluid can pass between the adjacent zones, but if the contact is not ensured the interfaces are treated as walls. The nodes of the moving cell zone change their position, but the cells defined by these nodes keep their shape without deformation. This procedure provided a sliding interface, and allowed the motion decoupling of the two fluid cylinders in the present work. The grid is thus composed by a stationary region and a rotating region.

An unsteady simulation with the moving mesh technique works as a series of static simulations. For each time step, a certain number of iterations are performed with the mesh in its initial position. Then the moving region rotates rigidly around a specified axis of an angle function of the time step size and of the rotational speed of the moving mesh. The transient calculation starts again in the new static position. This angle is equal to the one that the turbine sweeps with its rotational speed value within that particular time step. So each time step can be correlated to a swept angle.

A moving mesh captures the transient aspect of the flow ensuring a more realistic analysis. If a non-uniform flow field is considered, for example as a consequence of a EOG, every cell center in the control volume is characterized by a different velocity in space and time $u(z,t)$. So, if MRF was applied in this case, the real flow behaviour wouldn't be appreciated, and the blade-fluid interaction would be misunderstood. This is because any radial position of the blade would actually stand still at constant z and interact with a relative velocity varying due both to the external conditions and to the virtual rotation.

With periodic boundaries the 180° geometrical symmetry is enhanced. In the steady validation this approximation together with MRF granted excellent results with less computational effort. However in the unsteady situation the symmetry assumptions made before are violated. The gust conditions are inherently asymmetrical due to the presence of a velocity profile varying with height z at the inlet section. The non-uniformity of the flow field also makes the mutual influence between the two blades not negligible, because of the different aerodynamic action on each one.

User Defined Function

Fluent allows to define several User Defined Functions (UDF) to impose boundary conditions or physical properties, both in steady or time-dependant conditions [34]. In this case a suitable combination of two UDFs was used to properly represent the gust velocity profile at the inlet section. A first UDF is used to initialize the flow field and comprehends the normal wind profile $u(z)$ as the situation before the gust event. A second UDF models the EOG itself, $u(z,t)$. The implemented equations are reported in Chapter 4.

Once written in C language and compiled in Fluent, both the UDFs became selectable options in the boundary conditions panel. If Fluent is running in parallel mode, it's necessary to use the *compiled UDF* option, because of compatibility issues between parallel solver settings and the *interpreted UDF*. Therefore the *udf.c* file was imported as the *source* file, while the *header* file *udf.h* was found in the Fluent installation folder. In unsteady CFD terms, the variable t corresponds to a general time step in the time-marching process, and T is the total simulated time with the unsteady solver, or the steps number times their size. Since a turbine rotation is completed in about 0.83 s, in $T = 10.5$ s more than 12 complete rotations are included.

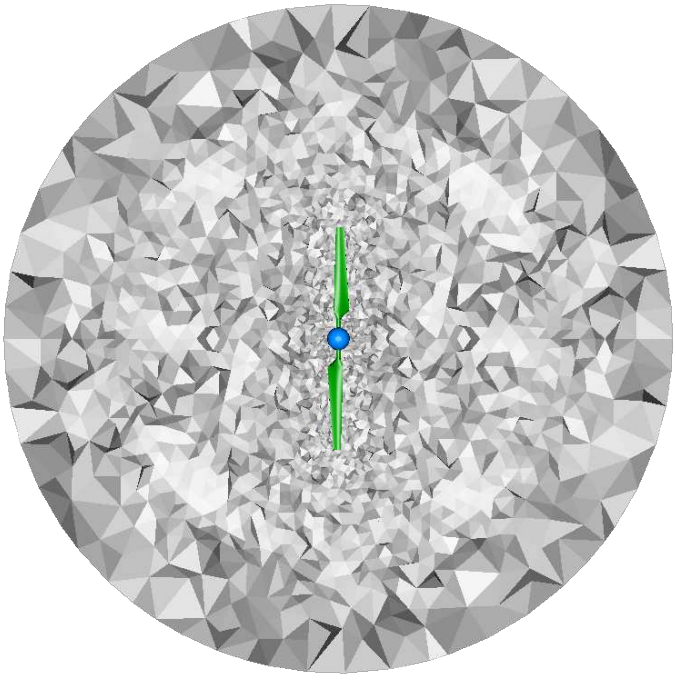

Figure 5.2: *mesh cross-section near $y = 0$, downwind view.*

Solver setup

For the operative case two different mesh files were exported from Pointwise, a stator domain file and a rotor domain file. The rotor file was associated to the stator one in Fluent with the *append case* function, and *interface mesh* surfaces were created. To define a mesh interface, two surface conditions have to be coupled. Thanks to the procedure explained before, 6 surfaces were available. Therefore 3 mesh interfaces were created, coupling the front, the rear and the lateral cylindrical surfaces. To grant the software stability it is important to follow an order while creating the three interfaces. So, if the first interface is created by selecting an outer domain surface as *interface zone 1* and an inner domain surface as *interface zone 2*, the next interfaces should be created with the same selection order. In this way, although the two meshes are independent, they are coupled at the interfaces, allowing coherent rotation of the rotor zone and flow passage between the zones. For the parked case instead no movement occurs.

Again, $k-\omega$ SST model was applied. The boundary conditions for the rotor surfaces were set to *no slip wall* with moving option, and no relative velocity with the adjacent cells. Turbulent intensity at the inlet and outlet sections was kept to the standard value of 5% to take in account the increased turbulence compared to the wind tunnel conditions. To give a proper initialization to the transient simulation, 1000 steady iterations with MRF option and the steady UDF profile $u(z)$ as inlet boundary condition were performed. Hence the flow field before the gust event was modelled, namely the steady situation with $t < 0$ of Figure 4.2. A wind speed of $u_{hub} = 25\ m/s$ was chosen. The turbine rotational speed of the operative case is 72.162 rpm, like in the 25 m/s validation case. The *pressure-based* solver with *coupled* algorithm was employed. After the flow initialization, *implicit second order* unsteady solver was engaged, and the moving mesh zone condition was activated. The unsteady UDF profile $u(z,t)$ was set for the inlet condition. A maximum Courant number of 200, explicit relaxation factors of 0.75 and 10^{-5} residuals were used. A moment monitor was set to detect the net torque signal $M_y(t)$ for each time step.

To reduce the simulation required time, a variable time step method was applied. Time step size is directly related to a swept angle, as explained before. So for each time step the rotating mesh zone switches forward of the corresponding swept angle. To avoid numerical fluctuations and convergence issues, a good choice is to match longer time steps with lower wind speeds and vice versa. For these reasons the time step size was progressively reduced while reaching the gust peak, and then increased after the event, like explained in Table 5.1. After a sensibility analysis, the reported values of time step sizes and number of steps were used. Time steps of 2.5° were imposed at the gust ends, to speed up the simulation in the first and last three seconds of virtual time without convergence consequences. 1° is adopted around the peak zone, and auxiliary time steps of 1.5° and 2° were included in between to ensure a gradual change. In fact an abrupt variation of time step size may cause divergence. For each time step, a maximum of 50 iterations was set.

Unsteady results

Loads

The aerodynamic torque $M_y(t)$ monitored during the simulations is reported in Figure 5.3. The thick lines come from a 20 points interpolation, which captures the average shape, whereas the thin lines represent the instant values. The trend reflects the wind gust profile. For the operating turbine, coming from 25 m/s, the first value for $t = 0$ s agrees with the torque result of the steady case with the same speed. The effect lowers, and after the peak the trend continues almost in a symmetrical way, restoring the initial value at $t = 10.5$ s. Within 2 seconds from $t = 3$ s the aerodynamic torque experiences a steep enhancement, with an increase of about 60% from the beginning. This strong gradient is of interest for structural ultimate and fatigue analyses of both the blade and the shaft.

The torque of the parked turbine instead is 30% lower for all the wind speeds, due to the reduced lift effect generated on the blade. The general trend remains the same, and the main difference with the previous case is in the moment direction. In fact the moment axis points towards $y > 0$, the opposite if compared to the rotating case. With a tip pitch of 90°, the wind hits the suction side of the inboard region of the blade, bringing high pressure, and causing a moment in clockwise direction, seen from upwind.

angle [°]	step size [ms]	steps	time [s]
2.5	5.787	630	3.646
2.0	4.630	63	3.938
1.5	3.472	84	4.229
1.0	2.315	882	6.271
1.5	3.472	84	6.563
2.0	4.630	63	6.854
2.5	5.787	630	10.500

Table 5.1: *different time steps used in the unsteady simulation.*

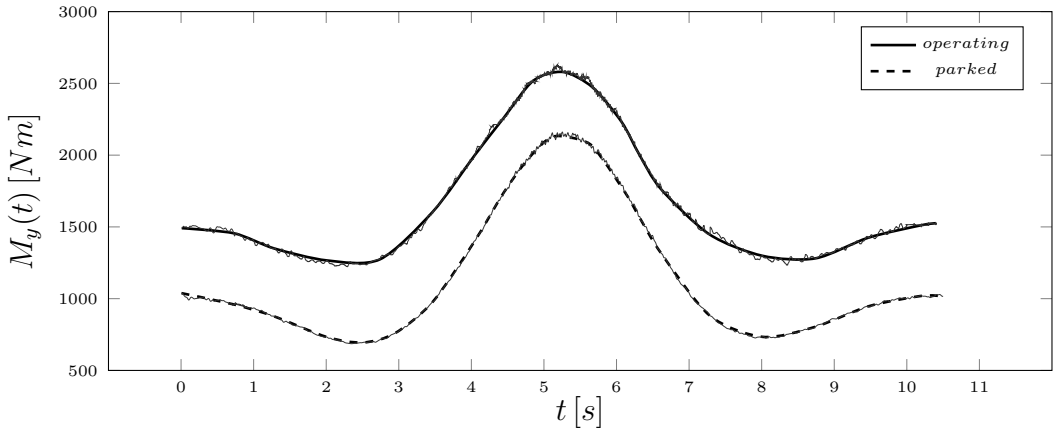

Figure 5.3: *aerodynamic torque around y axis for the two cases.*

The results of the bending and axial loads at the root section are here discussed. The blade model considered is rigid, therefore no displacement is taken in account. For more detailed load calculations, with fatigue and strain assessment, an aeroelastic Finite Element Model (FEM) is suggested [35]. The root section, located at $r_0 = 0.508\ m$ from the rotational center, has to bear the bending moments generated by the interaction with the airflow and by the rotation. In fact these moments reach there their maximum radial value, thus particular attention has to be paid in the design process. During the unsteady simulations 20 results files were saved, and with the *report* option Fluent allowed to print aerodynamic forces and moments acting on the wall surfaces for specified axes. Values where then interpolated every $\Delta\gamma = 30°$, averaging the aerodynamic effect on the two blades. The process was necessary to treat correctly the gravitational and centrifugal loads, which oscillate with the period of rotation. The blade was divided into 12 volumes resulting from the pattern of surfaces. Each element within two span positions was treated as a point of mass $m(r)$ at a radial distance r equal to the resulting center of mass [6].

In Figure 5.4 the flapwise bending moment around x axis $M_{xx}(t)$ is plotted for the root section of the rotating turbine. This variable depends only on the flow kinetic energy, which creates the thrust force. Due to its purely aerodynamic cause, the curve reflects the gust shape, with the slow oscillation period of the gust. A real blade would bend in downwind direction, so even gravitational and inertial forces would influence the result according to γ. From an initial value of 4.60 kNm, the maximum registered moment is 7.16 kNm. The maximum value reached by the parked turbine instead is barely 0.12 kNm, thanks to the small projected area exposed to the incoming wind, which minimizes the thrust force. This is a great contribution for a lower stress at the root section.

In Figure 5.5 the root edgewise bending moment around y axis $M_{yy}(t)$ is reported. In the rotating case this moment is composed by the sum of two components. The radial distribution of aerodynamic forces tangential to the rotational plane are transferred at the root section in terms of bending moment towards the direction of rotation. The second component is the gravitational force $\int_{r_0}^{R} m(r)gdr$, whose direction is constant during the blade rotation, therefore its tangential projection varies with $\sin(\gamma)$. For this reason the maximum bending due to gravity occurs for $\gamma = \pm 90°$. The combination gives a moment curve which oscillates with two periods, the turbine rotational period of 0.83 s for the gravitational force, and the gust period of 10.5 s for the aerodynamic forces. The higher value reached is 2.29 kNm. Conversely, the moment of the parked turbine shows only the gust period, due to the lack of gravitational effects, with a maximum of 1.07 kNm.

The load in the radial direction, or the axial direction z of the local reference frame, is shown in Figure 5.6. Even $F_z(t)$ is composed of two contributions, that is gravity and centrifugal force. The former behaves in as explained for the edgewise moment, and oscillates with $\cos(\gamma)$, whereas the latter generates a constant bias equal to $\int_{r_0}^{R} m(r)\omega^2 r dr$. In fact the centrifugal force vector is parallel to the blade axis. The aerodynamic forces projection is axial direction is negligible, thus only the turbine period is relevant for the $F_z(t)$ oscillations. The maximum load occurs for $\gamma = 180°$, when the two forces combine, and the minimum is then located at $\gamma = 0°$. For the operating turbine the overall load is tensile, dominated by the centrifugal force of 7.35 kN, with the fluctuating gravitational component of $\pm 0.56\ kN$. For the parked case instead only gravity stands, with opposite effect on each blade, so the stress at the root is constant and strongly reduced.

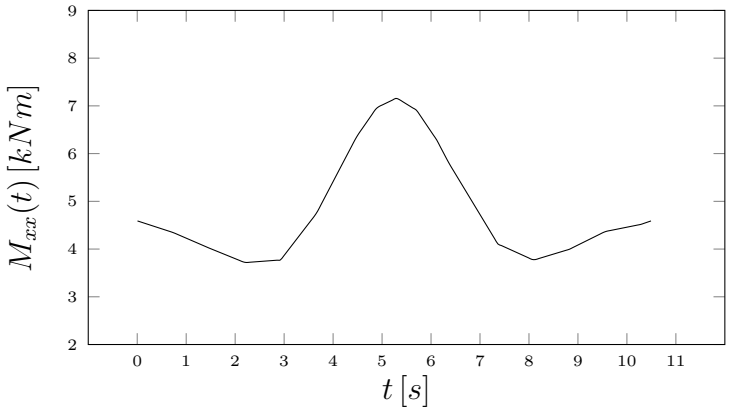

Figure 5.4: *root flapwise bending moment evolution for the operating turbine.*

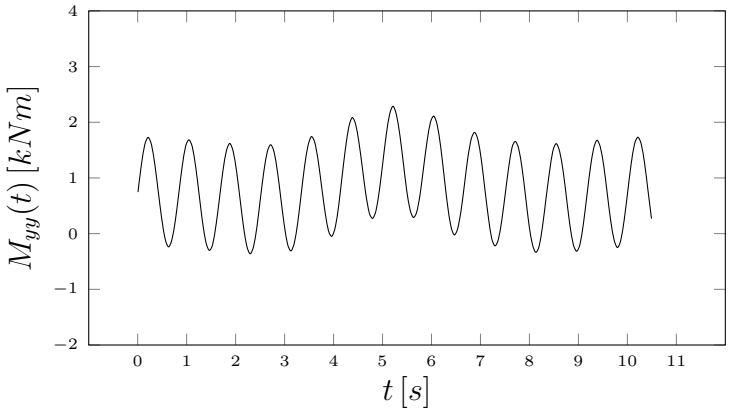

Figure 5.5: *root edgewise bending moment evolution for the operating turbine.*

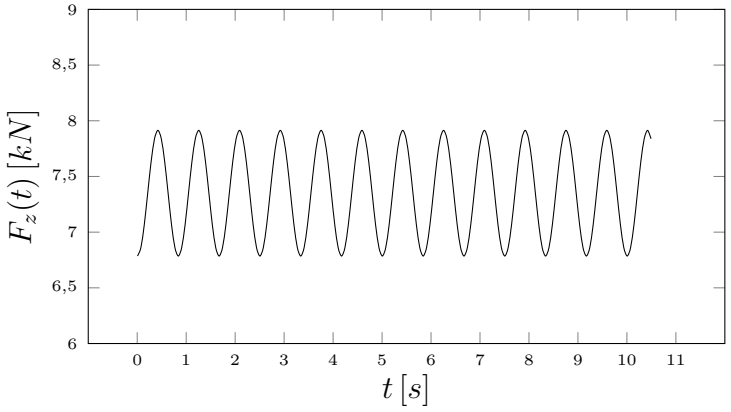

Figure 5.6: *axial load evolution for the operating turbine.*

According to the IEC 61400-2 standard presented in Chapter 4, the bending and axial loads were converted to stresses σ_M, σ_z and then in σ_{eq}, following Equations 4.10 - 4.12. For the calculation of flexural modulus W and surface A of the root section, an hypothesis had to be introduced, due to the lack of useful data concerning the internal blade structure. The known informations are the root shape, which is circular, and its external diameter $D = 21.8\ cm$. A shell thickness of 1.5 cm was then supposed.

Results regarding the evolution in time of the equivalent stress at the root section, $\sigma_{eq}(t)$, are reported in Figure 5.7, for the analysed cases. As can be seen for the operating turbine, the average value is mainly caused to the flapwise bending moment, whereas the smaller fluctuations derive from the other two loads. The equivalent stress ranges between 8.94 MPa and 17.23 MPa. The oscillations involved suggest also the importance of a fatigue assessment, not treated in this analysis.

About the parked turbine, the benefit resulting from the safety position is remarkable. The far lower equivalent stress stands between 0.87 MPa and 2.42 MPa, that is 10% - 15% of the previous case. Moreover short-term fluctuations are avoided. The most important contribution comes from the edgewise bending moment. This variable becomes dominant for the parked turbine, due to the drop of the flapwise moment and the axial load.

In the end, considering the partial safety factors proposed by the standard, which are $\gamma_M = 3.0$ for material not completely characterized, whose properties are known only from coupon testing, and $\gamma_L = 3.0$ for the extrapolation of stresses from load measurements, the ultimate strength of the composite material needs to be at least $\sigma_U = 155.07\ MPa$. This regards the most critical case, that is the rotating turbine. The present work adopted the EOG model with $N = 1$ as a representative gust shape, but if design purposes are involved, the use of EOG with $N = 50$ and $T = 14\ s$ is suggested by the standard.

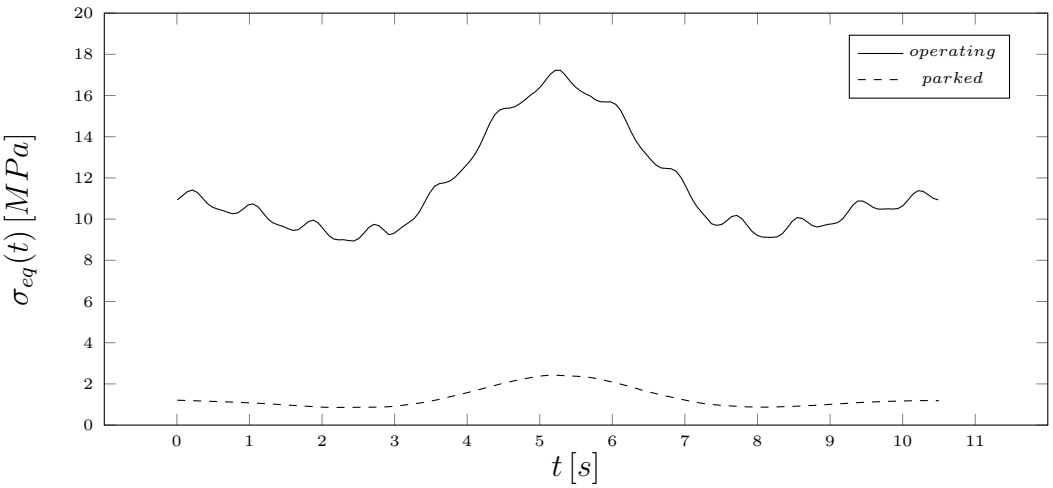

Figure 5.7: *equivalent stresses for the two cases according to IEC 61400-2* [33].

Pressure contours

Of the 20 saved cases, three relevant situations are now discussed in terms of pressure fields on the blade surfaces. The blades are depicted in vertical position but are associated to various azimuth angles. Figures 5.10 and 5.11 refer to the same azimuth $\gamma = -45°$ and to the different instants $t = 0.729\ s$, at the very beginning of the gust, and $t = 5.282\ s$, around the gust peak. The increased values near the leading edge of the pressure side, especially for the outboard region, are due to the higher attack angle and incoming relative speed. Thus the stagnation pressure increases too, because of the greater flow kinetic energy. This corresponds to a enhanced thrust force, and then to the flapwise bending moment peak discussed before.

The increased α between the two different instants is supposed to create a more abrupt flow separation, which results in a lower pressure at the suction side. Near the leading edge the effect is clearly visible, where the low pressure peak can be noticed too. However the pressure decreases more in the inboard region of the blade, where the higher turbulence and wider vortices are expected to be found.

The third case considered is explained by Figures 5.12 and 5.13, and corresponds to $t = 2.917\ s$, so within the wind velocity drop. The first and the second blade are analysed at the same instant in order to study the influence of the different γ, or the different height z. Both pressure sides and suction sides show a very similar trend. The main difference is a slightly greater pressure difference for the upper blade than the lower one, because the incoming velocity profile increases with z. However the overall behaviour is the same, so the averaging process from a set of 20 cases is considered to give a good approximation of the complete trend.

Streamlines

The streamlines of the airflow surrounding the 0.47 and 0.80 span positions were studied. In Figures 5.8 and 5.9 the tangential projection of the streamlines are depicted. The three representative cases cited above were analysed, so with different azimuth angles and wind speeds, but no relevant differences were noticed concerning the flow streamlines. It may be caused by the deeply stalled operation during all the simulated gust, so that no great variations occur in the simulated flow behaviour. For 0.47 span a wide vortex system is visible in the downwind region. Strong separation and turbulence is expected over the suction side, with a great flow reversion. A first vortex seems to start from the leading edge, joining a second opposite vortex which generates from the pressure side airflow, and then coming back to the suction side trailing edge. At 0.80 span such recirculation is reduced, as can be seen, probably due to the lower α.

With the adopted settings the steady validation is surely more suitable for fluid dynamics considerations, due to the stall development along the radius for an increasing velocity, whereas the unsteady simulation suggests a more structural character. It would be of great interest the coupled analysis of a wind gust ranging within the critical stall velocities, both from aerodynamic and structural purposes.

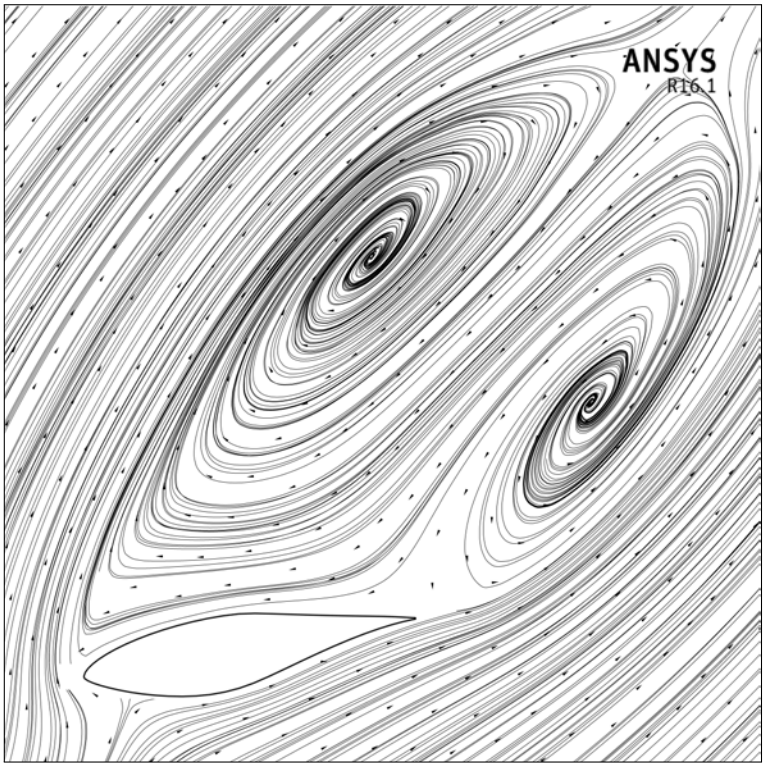

Figure 5.8: *streamlines, $\gamma = -45°$, 0.47 span projection.*

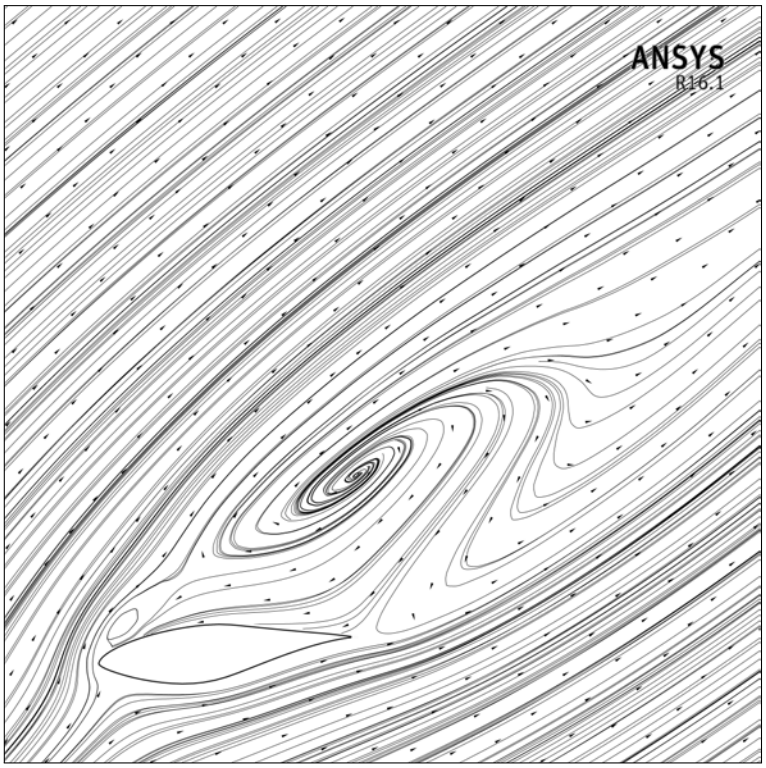

Figure 5.9: *streamlines, $\gamma = -45°$, 0.80 span projection.*

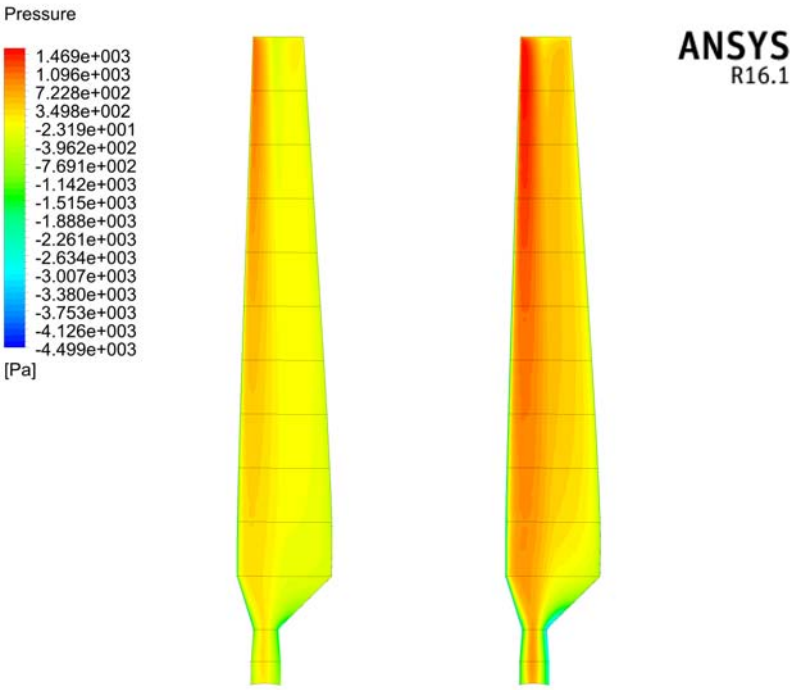

Figure 5.10: *pressure side contour,* $\gamma = -45°$*, for* $t = 0.729\ s$ *and* $t = 5.282\ s$*.*

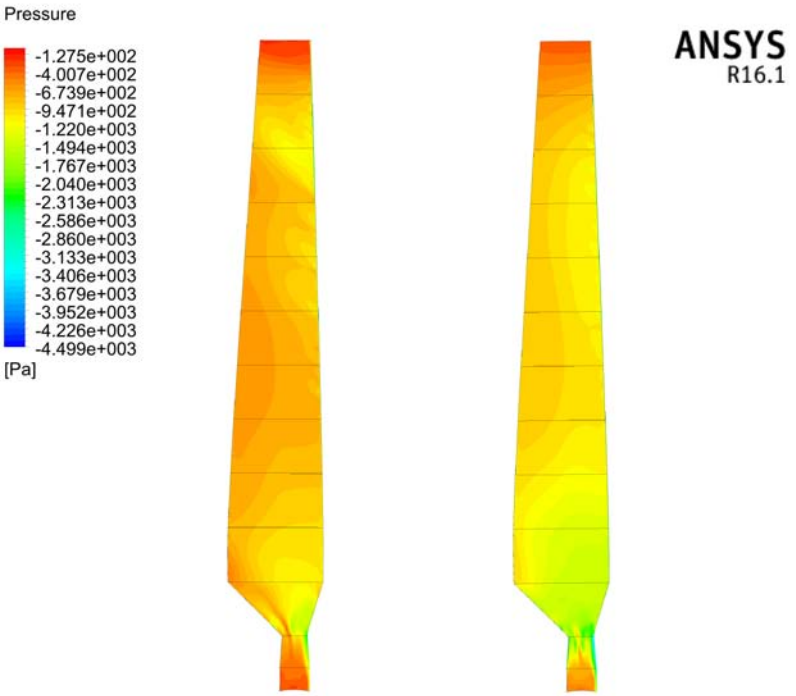

Figure 5.11: *suction side contour,* $\gamma = -45°$*, for* $t = 0.729\ s$ *and* $t = 5.282\ s$*.*

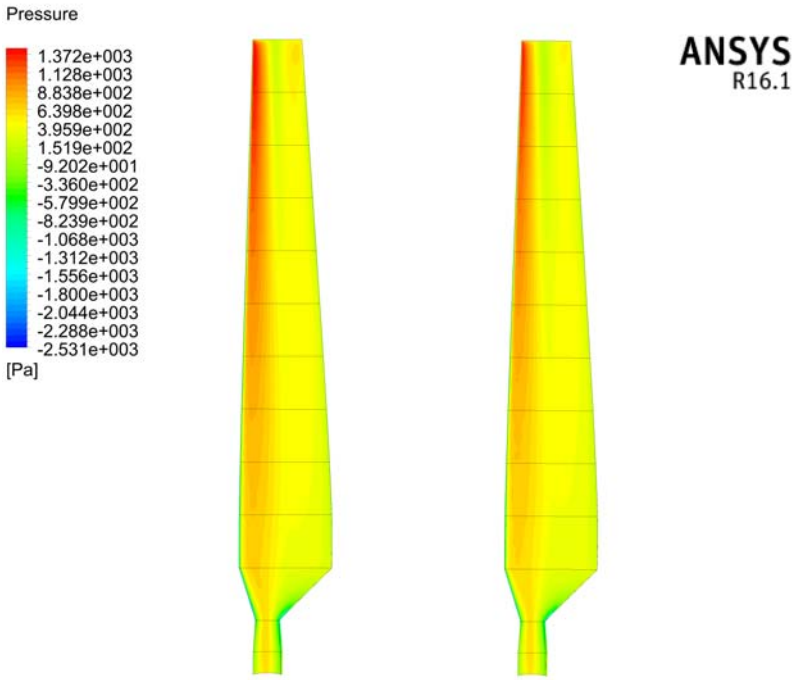

Figure 5.12: *pressure side contour,* $t = 2.917$ *s, for* $\gamma = 0°$ *and* $\gamma = 180°$.

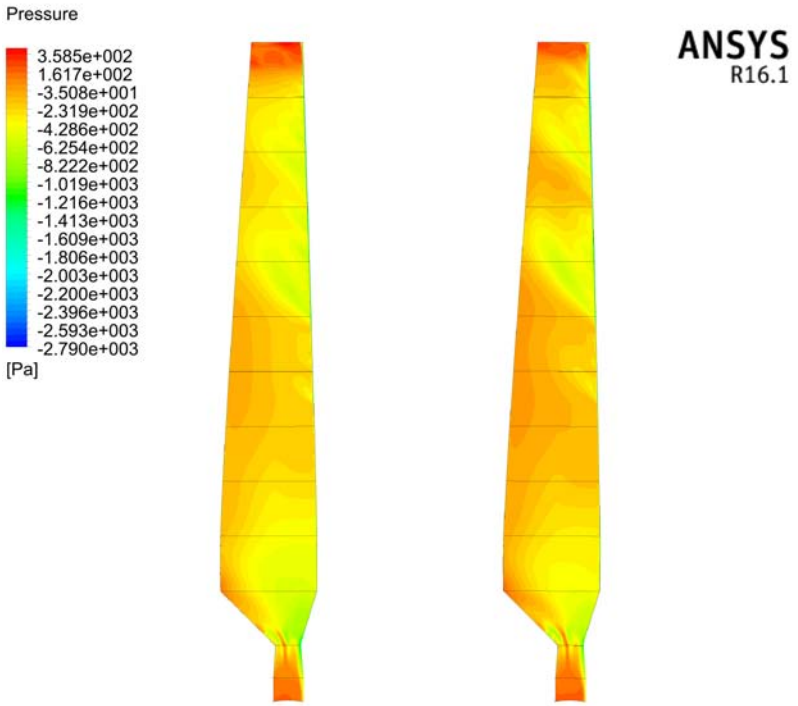

Figure 5.13: *suction side contour,* $t = 2.917$ *s, for* $\gamma = 0°$ *and* $\gamma = 180°$.

Conclusions

A wind turbine model has been discussed and successfully validated with a numerical CFD analysis and the comparison with experimental data. The results of pressure, velocity field, stall development and torque have been confirmed. The MRF approach granted in the end a very good approximation. Then the behaviour of the turbine operating in unsteady conditions has been presented together with the results of the transient simulation. The moving mesh technique had to be adopted, despite its high computational cost. A well characterized wind gust model from IEC 61400-2 standard was chosen, and two load cases have been suggested, that is turbine in undisturbed operation and parked turbine. The evolution in time of bending moments, axial load and consequent stresses at the root section have been reported, and an overall coherent trend is noticed. The benefit of feathering the turbine blades has been pointed out in terms of lower stress transferred to the critical root section.

The CFD approach seems to be a reliable solution to study 3D phenomena, which affect the wind turbines during their operation, relying only on a rather small amount of experimental data. The steps followed in the present work showed that interesting fluid dynamics observations arise mostly from the steady validation, whereas the unsteady results are more likely to be considered for a structural approach. Next works may research on the combined effect of a wind gust ranging within the critical wind speeds for the stall development. The use of an aeroelastic code would grant useful results both for stall-induced vibrations, extreme deformations and fatigue assessment. Unsteady analyses focused on the evolution of the wake vortices in a simulated ABL environment could lead to meaningful aerodynamic and aeroacoustic conclusions.

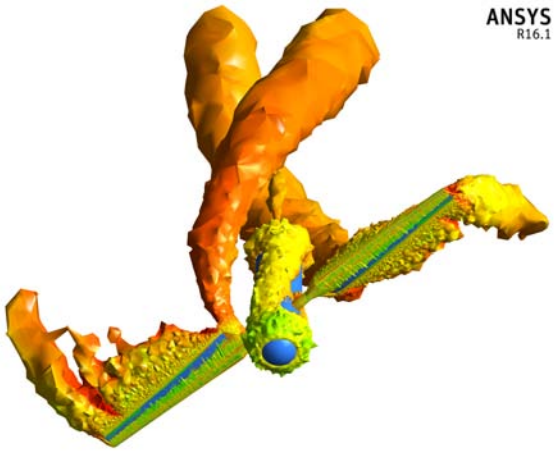

Near wake structure. Vortices released from tip and root regions at $t = 10.5$ s of the unsteady simulation, obtained with the method of the second invariant of the velocity gradient tensor, or Q criterion. Colours over the iso-Q surface show the turbulent kinetic energy in logarithmic scale.

Appendix A

S809 airfoil

This NREL airfoil had been designed specifically for HAWT applications. Its shape, plotted in A.1, is defined by a spline of points with coordinates reported in Table A.1 [6]. Three main characteristics are briefly underlined below. Further explainations and experimental results to prove these features are documented in the S809 design report [36].

- *Low maximum lift coefficient*: a quite sharp leading edge determines a high favourable pressure gradient, whose effect is a low pressure peak for high lift coefficients C_L. This peak restrains the maximum lift, and sets the flow transition point just after the leading edge for both airfoil sides. Consequently the maximum C_L values occur when nearly the entire profile is surrounded by turbulent flow. Therefore a noticeable C_L loss due to transition is avoided, and there's also a limited influence of roughness on the airfoil performance.

- *Low profile-drag coefficient*: a favourable pressure gradient up to 50% of chord lenght for suction side, and 40% for pressure side, is required in order to achieve low profile-drag. The following little adverse pressure zone ensures the flow attachment, and the final stronger adverse pressure results in a lower drag coefficient for the airfoil.

- *Soft stall development*: as a consequence of the previous explainations, and thanks to a rather high maximum thikness of 21%, stall occurs without abrupt separation, starting from the leading edge region of the suction side.

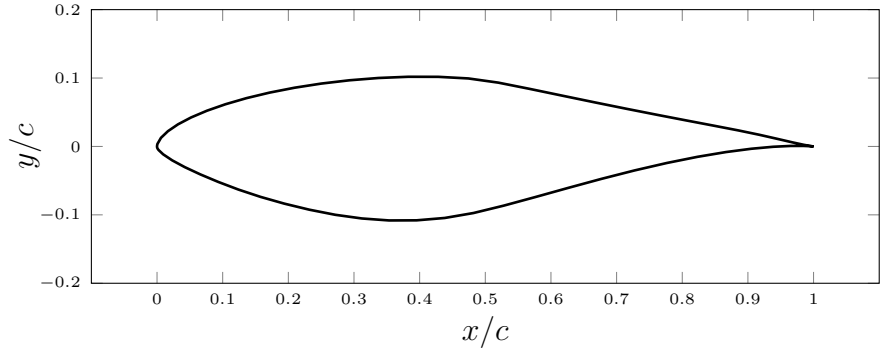

A.1: *S809 airfoil shape, coordinates normalized with chord lenght c.*

x/c	y/c	x/c	y/c
1.000000	0.000000	0.000213	-0.001794
0.996203	0.000487	0.001045	-0.003477
0.985190	0.002373	0.001208	-0.003724
0.967844	0.005960	0.002398	-0.005266
0.945073	0.011024	0.009313	-0.011499
0.917488	0.017033	0.023230	-0.020399
0.885293	0.023458	0.042320	-0.030269
0.848455	0.030280	0.065877	-0.040821
0.807470	0.037766	0.093426	-0.051923
0.763042	0.045974	0.124111	-0.063082
0.715952	0.054872	0.157653	-0.073730
0.667064	0.064353	0.193738	-0.083567
0.617331	0.074214	0.231914	-0.092442
0.567830	0.084095	0.271438	-0.099905
0.519832	0.093268	0.311968	-0.105281
0.474243	0.099392	0.353370	-0.108181
0.428461	0.101760	0.395329	-0.108011
0.382612	0.101840	0.438273	-0.104552
0.337260	0.100070	0.481920	-0.097347
0.292970	0.096703	0.527928	-0.086571
0.250247	0.091908	0.576211	-0.073979
0.209576	0.085851	0.626092	-0.060644
0.171409	0.078687	0.676744	-0.047441
0.136174	0.070580	0.727211	-0.035100
0.104263	0.061697	0.776432	-0.024204
0.076035	0.052224	0.823285	-0.015163
0.051823	0.042352	0.866630	-0.008204
0.031910	0.032299	0.905365	-0.003363
0.016590	0.022290	0.938474	-0.000487
0.006026	0.012615	0.965086	0.0007430
0.000658	0.003723	0.984478	0.0007750
0.000204	0.001942	0.996141	0.0002900
0.000000	-0.00002	1.000000	0.0000000

Table A.1: *S809 airfoil coordinates, normalized with chord lenght c* [6].

Bibliography

[1] *WWEA Half Year Report*, WWEA, 2016.

[2] *Key World Energy Statistics*, IEA, 2016.

[3] J. F. Manwell, J. G. McGowan, A. L. Rogers, *Wind Energy Explained - Theory, Design and Application*, John Wiley & Sons, 2002.

[4] T. Burton, D. Sharpe, N. Jenkins, E. Bossanyi, *Wind Energy Handbook*, John Wiley & Sons, 2001.

[5] M. O. L. Hansen, *Aerodynamics of Wind Turbines*, second edition, Earthscan, 2008.

[6] M.M. Hand, D.A. Simms, L.J. Fingersh, D.W. Jager, J.R. Cotrell, S. Schreck, S.M. Larwood, *Unsteady Aerodynamics Experiment Phase VI: Wind Tunnel Test Configurations and Available Data Campaigns*, NREL report, 2001.

[7] D. Simms S. Schreck M. Hand L.J. Fingersh, *NREL Unsteady Aerodynamics Experiment in the NASA-Ames Wind Tunnel: A Comparison of Predictions to Measurements*, NREL report, 2001.

[8] J. Mo, Y. Lee, *CFD Investigation on the aerodynamic characteristics of a small-sized wind turbine of NREL PHASE VI operating with a stall-regulated method*, Journal of Mechanical Science and Technology, 2012.

[9] N. N. Sørensen, J. A. Michelsen, S. Schreck, *Navier–Stokes Predictions of the NREL Phase VI Rotor in the NASA Ames 80 ft ð 120 ft Wind Tunnel*, Wind Energy, 2002.

[10] A. Le Pape, J. Lecanu, *3D Navier–Stokes Computations of a Stall-regulated Wind Turbine*, Wind Energy, 2004.

[11] M. M. Yelmule, E. Anjuri, *CFD predictions of NREL Phase VI Rotor Experiments in NASA/AMES Wind tunnel*, International Journal of Renewable Energy Resarch, 2013.

[12] J. C. Huang, H. Lin, T. Y. Hsieh, J. Y. Yang, *Aerodynamic Analysis of Wind Turbines Rotors with High Lift Airfoils by Using Pre-conditioned WENO Scheme*, Seventh International Conference on Computational Fluid Dynamics (ICCFD7), 2012.

[13] N. Sezer-Uzol, L. N. Long, *3-D Time-Accurate CFD Simulations of Wind Turbine Rotor Flow Fields*, AIAA paper no. 0394, 2006.

[14] Y. Song, J. B. Perot, *CFD Simulation of the NREL Phase VI Rotor*, Master Theses May 2014, 2014.

[15] Y. A. Cengel, J. M. Cimbala *Meccanica dei fluidi*, second edition, Mc Graw-Hill, 2011.

[16] A. Dal Monte, *Introduction to Computational Fluid Dynamic*, Progetto di Macchine, course material, Università degli Studi di Padova, 2016.

[17] K. Hanjalić, *Closure Models for Incompressible Turbulent Flows*, Introduction to the Modelling of Turbulence, Von Karman Institute, 2004.

[18] *ANSYS Fluent Theory Guide*, ANSYS Inc., 2013.

[19] *ANSYS Fluent User's Guide*, ANSYS Inc., 2013.

[20] B. S. Gerber, J.L. Tanger, E. P. N. Duque, J. D. Kocurek, *Peak and Post-Peak Power Aerodynamics from Phase VI NASA Ames Wind Turbine Data*, Journal of Solar Energy Engineering, 2005.

[21] A. Gonzalez, X. Munduate, *Three-Dimensional and Rotational Aerodynamics on the NREL Phase VI Wind Turbine Blade*, Journal of Solar Energy Engineering, 2008.

[22] S. Tonio, V. K. Gijs, V. B. Gerard, *Estimating the Unsteady Angle of Attack from Blade Pressure Measurements on the NREL Phase VI Rotor in Yaw using a Free-Wake Vortex Model*, 44th AIAA Aerospace Science Meeting and Exhibit, 2006.

[23] J. Tangler, J. D. Kocurek, *Wind Turbine Post-Stall Airfoil Performance Characteristics Guidelines for Blade-Element Momentum Methods*, NREL report, 2004.

[24] N. Z. Ahmed, *Comparative study of wind gusts: detection techniques and terrain specific features*, Master of Science Thesis, Delft Univeristy of Technology, 2015.

[25] R. E. Bartels, *Development, Verification and Use of Gust Modeling in the NASA Computational Fluid Dynamics Code FUN3D*, NASA report, 2012.

[26] G. C. Larsen, W. Bierbooms, K. S. Hansen, *Mean Gust Shapes*, Risø National Laboratory, Technical University of Denmark, 2003.

[27] C. Knigge, S. Raasch, *Improvement and development of one- and two-dimensional discrete gust models using a large-eddy simulation model*, Journal of Wind Engineering and Industrial Aerodynamics, 2016.

[28] L. S. Seregina, R. Haas, K. Born, J. G. Pinto, *Development of a wind gust model to estimate gust speeds and their return period*, Tellus A: Dynamic Meteorology and Oceanography, International Meteorological Institute of Stockholm, 2014.

[29] J. Mann, *Atmospheric turbulence*, DTU Wind Energy, Technical University of Denmark, 2012.

[30] J. Grzędziński, A. Mróz, *Gust load reduction concept in wind turbines*, Wind Energy, 2010.

[31] R. C. Storey, S. E. Norris, J. E. Cater, *Modelling Turbine Loads during an Extreme Coherent Gust using Large Eddy Simulation*, Journal of Physics: Conference Series, 2010.

[32] V. Gutpa, *Aerodynamic and Structural Analyses of the 5 MW Wind Turbine Using BEM and Lifting Line Theories*, Master of Science Thesis, Delft Univeristy of Technology, 2012.

[33] IEC 61400-2:2006 International Standard, *Wind turbines: Design requirements for small wind turbines*, 2006.

[34] *ANSYS Fluent UDF Manual*, ANSYS Inc., 2013.

[35] H. J. Sutherland, J. F. Mandell, *Effect of Mean Stress on the Damage of Wind Turbine Blades*, Journal of Solar Energy Engineering, 2004.

[36] D. M. Somers, J. Tangler, *Design and Experimental Results for the S809 Airfoil*, NREL Report, 1997.

[37] M. Sherry, J. Sheridan, D. Lo Jacono, *Characterisation of a horizontal axis wind turbine's tip and root vortices*, Experiments in Fluids, 2013.

[38] L. Michelini, *Numerical Investigation of the Influence of both Length and Root Chord on the Aerodynamic Performance of a Tip-Mounted Winglet for HAWT Application*, Master of Science Thesis, Università degli Studi di Padova, 2013.